Birnessite polytype systematics and identification by powder X-ray diffraction

VICTOR A. DRITS,[1,2] BRUNO LANSON,[1,*] AND ANNE-CLAIRE GAILLOT[1]

[1]Environmental Geochemistry Group, LGIT—Maison des Géosciences, University of Grenoble—CNRS, 38041 Grenoble Cedex 9, France
[2]Geological Institute, Russian Academy of Sciences, 7 Pyzhevsky Street, 109017 Moscow, Russia

ABSTRACT

The polytypes of birnessite with a periodic stacking along the $\mathbf{c}^*$ axis of one-, two-, and three-layers are derived in terms of an anion close-packing formalism. Birnessite layers may be stacked so as to build two types of interlayers: P-type in which basal O atoms from adjacent layers coincide in projection along the $\mathbf{c}^*$ axis, thus forming interlayer prisms; and, O-type in which these O atoms form interlayer octahedra. The polytypes can be categorized into three groups that depend on the type of interlayers: polytypes consisting of homogeneous interlayers of O- or P-type, and polytypes in which both interlayer types alternate. Ideal birnessite layers can be described by a hexagonal unit cell ($a_h = b_h \approx 2.85$ Å and $\gamma = 120°$) or by an orthogonal C-centered cell ($a = \sqrt{3}\,b$, $b_h \approx 2.85$ Å, and $\gamma = 90°$); and, hexagonal birnessite polytypes ($1H$, $2H_1$, $2H_2$, $3R_1$, $3R_2$, $3H_1$, and $3H_2$) have orthogonal analogs ($1O$, $2O_1$, $2O_2$, $1M_1$, $1M_2$, $3O_1$, and $3O_2$).

X-ray diffraction (XRD) patterns from different polytypes having the same layer symmetry and the same number of layers per unit cell exhibit *hkl* reflections at identical 2θ positions. XRD patterns corresponding to such polytypes differ only by their *hkl* intensity distributions, thus leading to possible ambiguities in polytype identification. In addition, the characteristics of the birnessite XRD patterns depend not only on the layer stacking but also on the presence of vacant layer sites, and on the type, location, and local environment of interlayer cations.

Several structure models are described for birnessite consisting of orthogonal vacancy-free or of hexagonal vacancy-bearing layers. These models differ by their stacking modes and by their interlayer structures, which contain mono-, di-, or trivalent cations. Calculated XRD patterns for these models show that the *hkl* intensity distributions are determined by the polytype, with limited influence of the interlayer structure. Actual structures of phyllomanganates can thus be approximated by idealized models for polytype identification purpose. General rules for this identification are formulated. Finally, the occurrence of the different polytypes among natural and synthetic birnessite described in the literature is considered with special attention given to poorly understood structural and crystal-chemical features.

Keywords: Birnessite, polytype, phyllomanganate, Mn oxide

INTRODUCTION

Birnessite is a hydrous-layered Mn oxide (phyllomanganate). Its layers consist of edge-sharing MnO_6 octahedra and these layers are separated from each other by hydrated interlayer cations. These cations compensate for a layer charge deficit arising either from the presence of vacant layer sites or from the coexistence of heterovalent Mn cations in the octahedral layer. Birnessite interlayers incorporate a single sheet of interlayer H_2O molecules, and exhibit a minimum periodicity along the $\mathbf{c}^*$ axis of ~7 Å (Giovanoli et al. 1970a, 1970b; Burns and Burns 1977; Chukhrov et al. 1978; Post and Veblen 1990). In the following, the term "birnessite" will be used to describe all natural and synthetic materials with such a layer structure, whatever the origin of the layer charge, and the actual configuration and chemical composition of the interlayers.

Over the last few decades, birnessite has attracted a wide interest for several reasons. First, it is ubiquitous in geological environments in spite of the low abundance of Mn. It is, for example, a major component of Mn nodules, which cover huge areas of the ocean floor and the bottom of some lakes. It is also present in soils, sediments, and Mn-rich ore deposits (Burns and Burns 1977, 1978; Chukhrov et al. 1978, 1985; Drits et al. 1985; Golden et al. 1986; Cornell and Giovanoli 1988; Manceau et al. 2000c). It was recently shown that bacteria play a major role in the formation of birnessite in most of these environments (Tebo and He 1999; Tebo et al. 2004; and references therein). Second, this mineral plays an essential role in different ion-exchange and redox processes because of its unique surface charge, and adsorption and redox properties (Manceau and Charlet 1992; Manceau et al. 1992a, 1992b; Paterson et al. 1994; Stone et al. 1994; Tu et al. 1994; Le Goff et al. 1996; Silvester et al. 1997). In particular, birnessite plays a pivotal role in the fate of heavy metals and other pollutants in contaminated water systems and soils (Chao and Theobald 1976; Manceau et al. 1997, 1999, 2000a, 2000b). Despite its low abundance, birnessite controls

---

the distribution of some trace elements such as radionuclides, Pt-group elements, and rare-earth elements (Manceau et al. 1999). In addition, birnessite has also attracted special attention because of its potential use as materials for batteries and other industrial applications (Kim et al. 1999).

Third, birnessite can be synthesized under various physico-chemical conditions and from 0 to 1000 °C. Synthetic birnessite is used to mimic naturally occurring redox and adsorption processes, being considered as analogous to natural varieties. Birnessite can be synthesized by the oxidation of Mn^{2+} in a highly alkaline medium (Giovanoli et al. 1970a, 1970b; Cornell and Giovanoli 1988; Kim et al. 2000), leading, for example, to the topotactic transformation of $Mn(OH)_2$ when subjected to the action of different oxidizers. Other methods using MnO_4^- as a starting reagent (Herbstein et al. 1971; Ching et al. 1995, 1997a, 1997b; Chen et al. 1996a, 1996b; Ching and Suib 1997; Kim et al. 1999) include mild hydrothermal syntheses (Feng et al. 1995; Chen et al. 1996a, 1996b), sol-gel processes (Bach et al. 1990, 1993; Le Goff et al. 1994; Ching et al. 1995, 1997a; Cho et al. 1999), interactions of $KMnO_4$ with hydrochloric acid, and ion-exchange of the hydrogen form of birnessite to the Na- or K-forms (Tsuji et al. 1992; Leroux et al. 1995), and thermal decomposition of $KMnO_4$ at high temperature (Kim et al. 1999).

These different methods lead to the crystallization of birnessite having different layer stackings and different interlayer structures, which depend on the chemical nature of interlayer cations, their amounts, distribution, and coordination geometry. In addition, birnessite is, as a rule, fine-grained and contains stacking faults and/or consists of interstratified layer types corresponding to different birnessite polytypes (Drits et al. 1997a, 2002; Silvester et al. 1997; Manceau et al. 2000c, 2002; Lanson et al. 2002a, 2002b). As a result, strikingly different X-ray diffraction patterns are obtained from birnessite crystallized under different physico-chemical conditions. As a consequence, there has been a lot of confusion, even in the recent literature, as to the structure of these layer manganates (e.g., Chen et al. 1996b; Kim et al. 1999; Yang and Wang 2001). One difficulty in the interpretation of the birnessite XRD patterns is that, until recently, even unit-cell parameters reported in the literature were not determined unambiguously. Therefore, determination of the birnessite structure was sometimes limited to a general description of the XRD patterns without any indexing or accurate determination of unit-cell parameters (Feng et al. 1997a, 1997b; Aronson et al. 1999; Ma et al. 1999; Yang and Wang 2001). In some cases indexing of *hkl* reflections was carried out without proper justification (e.g., Le Goff et al. 1994, 1996; Ching et al. 1995; Aronson et al. 1999). Significant progress was achieved recently in the structural characterization of birnessite (Post and Veblen 1990; Kuma et al. 1994; Drits et al. 1997a, 1998, 2002; Manceau et al. 1997, 2000c, 2002; Silvester et al. 1997; Lanson et al. 2000, 2002a, 2002b) and specifically in the determination of their unit-cell parameters (Chen et al. 1996a, 1996b; Kim et al. 1999; Lanson et al. 2000, 2002a, 2002b). However, no systematic description of reliable criteria for the identification of birnessite polytypes is available, to our knowledge, in the existing literature.

As for layer silicates (Bailey 1988) the optimal way to establish such criteria is to deduce theoretically all birnessite polytypes taking into account the main crystal-chemical features of their layers and interlayers, to calculate the corresponding XRD patterns and to formulate diffraction criteria for their identification. This paper is devoted to such a systematic approach and describes how birnessite polytypes having the same unit-cell parameters can be identified.

BIRNESSITE POLYTYPE DIVERSITY

Polytype diversity in terms of close-packing formalism

The two-dimensional periodicity of birnessite layers can be described either by a hexagonal unit cell, with $a_h = b_h \approx 2.85$ Å and $\gamma = 120°$, or by an equivalent orthogonal C-centered cell, with $a = \sqrt{3}\,b$, $b_h \approx 2.85$ Å, and $\gamma = 90°$. The orthogonal C-centered cell will be used systematically throughout the current manuscript. The birnessite layer consists of two closely packed anion sheets "sandwiching" Mn cations. The anion close-packing formalism can thus be used to describe the mutual arrangement of birnessite layers. As a first step all possible periodic stackings of birnessite layers with periodicity along the **c** axis of 1, 2, and 3 layers will be considered. Non-equivalent crystallographic sites of the layer oxygen atoms (O_{layer}) will be hereafter described with capital letters A, B, and C, whereas positions of the Mn cations will be described with corresponding a, b, and c letters (Fig. 1). It is systematically assumed that the lower surface of the first birnessite layer is an oxygen sheet in which the the O_{layer} occupies A sites, that Mn cations fill octahedral b positions, and that the upper surface is formed by O_{layer} in C sites. Such a layer can be symbolically represented as AbC. In the simulation of idealized polytypes, it is assumed that the O_{layer} in the lower sheet of the next birnessite layer in a stack can occupy A, B or C positions. If these O_{layer} are located in C sites, O_{layer} from adjacent layers define interlayer prisms. This type of interlayer will be referred to as a P-type interlayer and denoted with an equal sign (=). If they are located in A or B sites, O_{layer} from adjacent layers define interlayer octahedra. These interlayers are referred to as O-type and denoted with a dash sign (–) to distinguish them from the P-type interlayers. Using the above notions, a one-layer polytype having O-type interlayer (Fig. 1a) can be represented as:

$$AbC - AbC... \quad 1H$$

Systematic consideration of possible two-layer polytypes leads to two independent hexagonal polytypes having homogeneous interlayers (Figs. 1b and 1c):

$$AbC = CbA = AbC... \quad 2H_1$$
$$AbC - AcB - AbC... \quad 2H_2$$
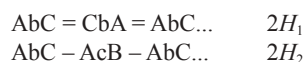
With this notation, the first digit indicates the number of layers per unit cell, the letter corresponds to the layer symmetry (*H*, *R*, and *M* standing for hexagonal, rhombohedral, and monoclinic, respectively), and the final numerical subscript determines the polytype. In $2H_1$ and $2H_2$ polytypes, adjacent layers are rotated with respect to each other by 180° around the axis parallel to the **c** axis and passing either through Mn atoms of adjacent layers ($2H_1$) or through the "lower" O_{layer} (A sites – $2H_2$). In $1H$ and $2H_1$, the Mn_{layer} octahedral sites overlap in projection on the **a-b** plane, whereas these sites are distributed more homogeneously in $2H_2$.

Analysis of three-layer polytypes leads to two independent modifications with rhombohedral symmetry (3*R*). These two
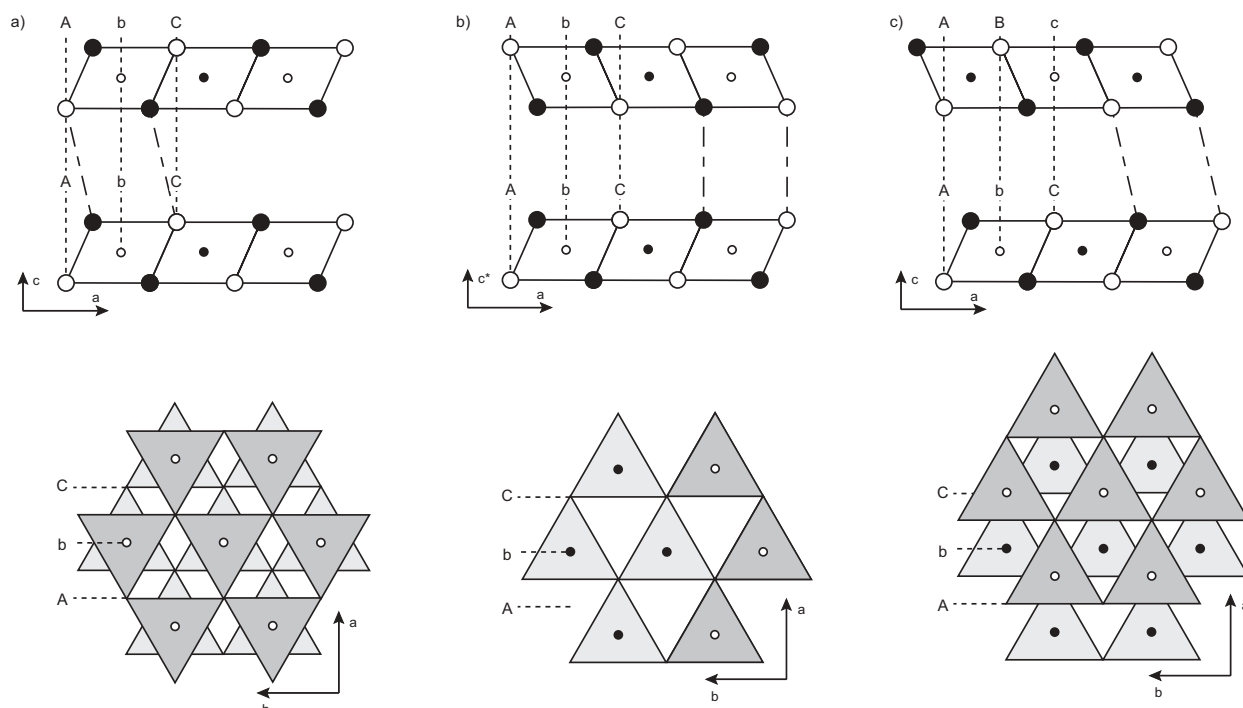
FIGURE 1. Idealized structure model of birnessite polytypes. (**a**) $1H$ polytype. Top: projection along the **b** axis. Open and solid symbols indicate atoms at $y = 0$ and $y = \pm\frac{1}{2}$, respectively. Large circles represent O_{layer} atoms and small circles represent Mn_{layer} atoms. Dashed lines outline specific positions of the close-packing formalism. Irregular dashed lines outline the interlayer octahedra defined by O_{layer} from adjacent layers. Bottom: projection on the **a-b** plane. The upper surface of the lower layer is shown as light-shaded triangles whereas the lower surface of the upper layer is shown as dark-shaded triangles. Mn_{layer} of the upper layer are shown as small open circles. (**b**) $2H_1$ polytype. Top: projection along the **b** axis. Irregular dashed lines outline the interlayer prisms defined by O_{layer} from adjacent layers. Bottom: projection on the **a-b** plane. Mn_{layer} of the lower layer are shown as small solid circles. Other symbols as in **a**. (**c**) $2H_2$ polytype. Top: projection along the **b** axis. Irregular dashed lines as in **a**. Bottom: projection on the **a-b** plane. Symbols and notations as in **a**.

polytypes differ from each other by their interlayer structures (Figs. 2a and 2b):

AbC = CaB = BcA = AbC... $3R_1$
AbC – BcA – CaB – AbC... $3R_2$
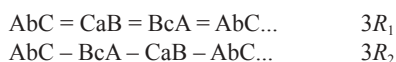
Two additional three-layer polytypes having O-type interlayers and hexagonal symmetry may also be derived (Figs. 2c and 2d):

AbC – AcB – AcB – AbC... $3H_1$
AbC – AcB – CaB – AbC... $3H_2$
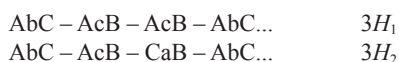
In terms of the C-centered orthogonal unit cell, successive layers in $3R_1$ and $3R_2$ polytypes are shifted by $-a/3$ and $+a/3$, respectively. As in $2H_2$ polytype, successive layers in $3H_1$ and $3H_2$ polytypes are not related by the same interlayer displacement. In addition, layers from different layer pairs are related to each other by different elements of symmetry in $3H_1$ and $3H_2$ polytypes. For example, layers in the first layer pair of the $3H_1$ polytype are related by a 180° rotation along the **c** axis passing through A sites, whereas they are superimposed in the second pair (Fig. 2c). In the latter layer pairs, Mn octahedral sites overlap in projection on the **a-b** plane, whereas in $3R_1$, $3R_2$, and $3H_2$ polytypes, layer Mn cations are distributed homogeneously among all possible sites (Figs. 2a, 2b, and 2d).

Heterogeneity arising from the coexistence of O- and P-

type interlayers in a given birnessite polytype is unlikely to be energetically favorable. Polytypes with alternating O- and P-type interlayers were thus excluded from the current study. However, transformation from one polytype to the other likely often occurs through layer translations. Such displacements occur, for example, as a result of cation exchange or during hydration-dehydration processes. Therefore, among birnessite polytypes some unusual modifications can be formed from one-layer polytype by shifting the layers. For example, a two-layer structure AbC – BcA = AbC with both interlayer types can be obtained if successive layers are shifted alternately by $+a/3$ and $-a/3$ along the **a** axis of the C-centered unit cell.

The above idealized birnessite polytypes are similar to those of oxides with the general formula A_xMO_2 (Delmas et al. 1980). These authors deduced four polytypes, T1, P2, P3, and O3, which correspond to $1H_1$, $2H_2$, $3R_1$, and $3R_2$ modifications in the present nomenclature. Birnessite polytypes are also similar to those of natural and synthetic layer double hydroxides $(R^{2+}_{1-x}R^{3+}_x)(OH)_2(CO_3,SO_4)_{x/2}$ (Drits 1987; Bookin and Drits 1993; Drits and Bookin 2001) and to those of other natural and synthetic layered compounds (Bailey 1980).

Layer symmetry and polytype diversity

Structural characterization of birnessite shows layers with either hexagonal or pseudo-hexagonal symmetry. Birnessite
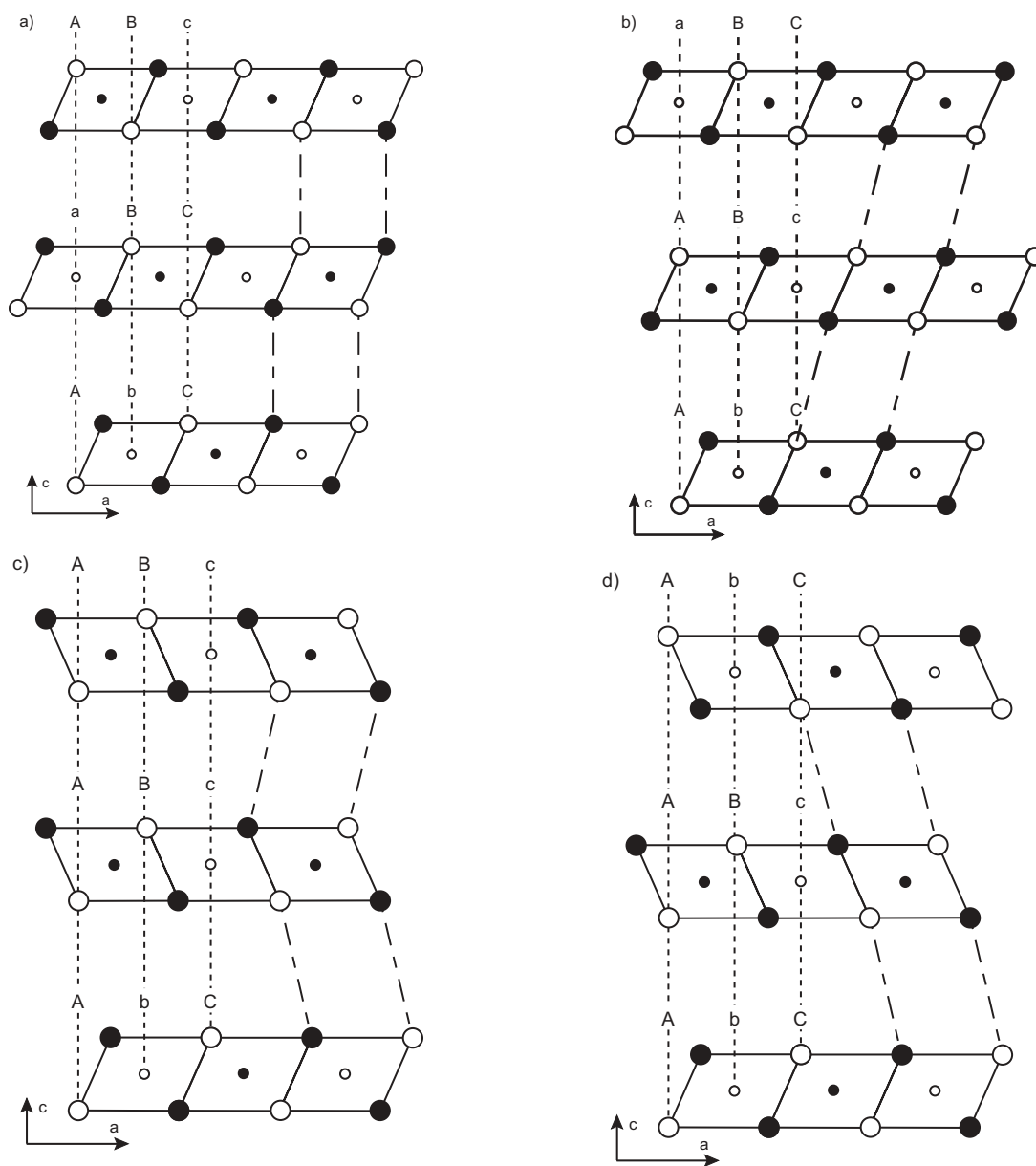
FIGURE 2. Idealized structure model of birnessite polytypes in projection along the **b** axis. (**a**) $3R_1$ polytype. Symbols and notations as in Figure 1. Irregular dashed lines outline the interlayer prisms defined by O_{layer} from adjacent layers. (**b**) $3R_2$ polytype. Irregular dashed lines outline the interlayer octahedra defined by O_{layer} from adjacent layers. (**c**) $3H_1$ polytype. Irregular dashed lines as in **b**. (**d**) $3H_2$ polytype. Irregular dashed lines as in **b**.

has an hexagonal layer symmetry when octahedral vacancies represent the major source of layer-charge deficit (Giovanoli et al. 1970b; Chukhrov et al. 1985; Silvester et al. 1997; Lanson et al. 2000, 2002b; Gaillot et al. 2003, 2005). By contrast, birnessite has an orthogonal layer symmetry when the main source of negative charge in vacancy-free layers is the presence of a high amount of Mn^{3+} cations (Post and Veblen 1990; Drits et al. 1998; Lanson et al. 2002a; Gaillot et al. 2004). In the latter case, the layers have a C-centered unit cell with $a > b\sqrt{3}$ (Burns and Burns 1977; Chukhrov et al. 1985; Post and Veblen 1990; Gorshkov et al. 1992; Drits et al. 1997a, 1998; Lanson et al. 2000, 2002a,

2002b; Gaillot et al. 2003, 2004, 2005). Orthogonal layer symmetry results from the distortion of Mn^{3+}-octahedra because of the Jahn-Teller effect (Drits et al. 1997a). In Mn^{3+} octahedra, two Mn^{3+}-O distances are indeed much longer than the other four. For example, in crednerite $CuMnO_2$ Mn^{3+}-octahedra contain two 2.26 Å and four 1.929 Å bond lengths with an average <Mn-O> distance of 2.04 Å (Töpfer et al. 1995). Similar distortions of Mn^{3+}-octahedra have been reported by Shannon et al. (1975) for α-MnOOH (2.041 Å—Glasser and Ingram 1968), γ-MnOOH (2.037 Å—Dachs 1963), and α-Mn_2O_3 (2.039–2.045 Å—Norrestam 1967). The random distribution of Mn^{4+} and Mn^{3+} cations

combined with a random azimutal orientation of the long Mn^{3+}-O bonds of the Mn^{3+} octahedra would lead to unfavorable steric strains, because of the distortion of Mn^{3+}-octahedra. An ordered distribution of Mn^{3+}-octahedra all having the same azimutal orientation allows minimization of these strains. According to SAED results, in vacancy-free birnessite layers, Mn^{3+} are distributed in rows parallel to the **b** axis and have their long Mn^{3+}-O bonds parallel to the **a** axis (Drits et al. 1997a, 1998; Lanson et al. 2002a; Gaillot et al. 2004). Because of the systematic elongation of Mn^{3+}-ocathedra along the **a** axis and because the four short Mn^{3+}-O distances (1.92–1.93 Å) are similar to Mn^{4+}-O bond lengths (1.912 Å for λ-MnO_2), b parameters are similar (2.83–2.85 Å) in most natural and synthetic birnessite samples regardless of the average valency of the Mn_{layer} (Chukhrov et al. 1985; Post and Veblen 1990; Chen et al. 1996b; Ching et al. 1997a; Drits et al. 1997a, 1998; Kim et al. 1999; Lanson et al. 2000, 2002a, 2002b; Gaillot et al. 2003, 2004, 2005).

The transition from birnessite having layers with hexagonal symmetry to that having pseudo-hexagonal symmetry leads to a modification of symbol notation for the corresponding polytypes. Specifically, hexagonal one-, two-, and three-layer polytypes ($1H$, $2H_1$, $2H_2$, $3H_1$, and $3H_2$) are changed to the corresponding orthogonal ones ($1O$, $2O_1$, $2O_2$, $3O_1$, and $3O_2$) whereas $3R_1$ and $3R_2$ are changed to $1M_1$ and $1M_2$ monoclinic modifications having $-a/3$ and $+a/3$ displacements of adjacent layers along the **a** axis (Table 1). In $1M_1$ and $1M_2$ birnessite, adjacent layers may be shifted along the **a** axis by values different from ±0.333a (Post and Veblen 1990; Lanson et al. 2002b).

Cation composition, interlayer structure, and polytype diversity

The arrangement of adjacent layers in different polytypes, the presence or absence of vacant layer octahedral sites, the nature of interlayer cations, and their local environments are interrelated structural characteristics. Therefore, it is reasonable to define possible interlayer structures for each particular layer stacking and specifically to propose optimum positions for interlayer cations as a function of their ionic radius and valence (Table 2). This approach also relies on existing birnessite structure models (Chukhrov et al. 1978, 1985; Post and Veblen 1990; Drits et al. 1997a, 1998, 2002; Kim et al. 1999; Lanson et al. 2000, 2002a, 2002b; Manceau et al. 2002; Gaillot et al. 2003, 2005). To symbolize positions for interlayer water molecules ($H_2O_{interlayer}$) and cations, the capital letters A', B', and C', and corresponding lower case a', b', and c' will be used, respectively.

Polytypes with hexagonal layer symmetry. The presence of layer vacancies allows interlayer cations to share one face with vacant octahedra so as to provide local charge compensation to

TABLE 1. List of possible periodic layer stacking modes in birnessite consisting of hexagonal (vacancy-bearing) or orthogonal (vacancy-free) layers

Layer stacking	Hexagonal layers	Orthogonal layers
AbC – AbC ...	$1H$	$1O$
AbC = CbA = AbC ...	$2H_1$	$2O_1$
AbC – AcB – AbC ...	$2H_2$	$2O_2$
AbC = CaB = BcA = AbC ...	$3R_1$	$1M_1$
AbC – BcA – CaB – AbC ...	$3R_2$	$1M_2$
AbC – AcB – AcB – AbC ...	$3H_1$	$3O_1$
AbC – AcB – CaB – AbC ...	$3H_2$	$3O_2$

undersaturated O_{layer}. If birnessite interlayers contain relatively small di- or trivalent cations, such as $Mn^{2+,3+}$, $Co^{2+,3+}$, Cu^{2+}, Ca^{2+}, and Mg^{2+}, then they are commonly octahedrally coordinated by O_{layer} bound to layer vacancies and $H_2O_{interlayer}$. Depending on the layer stacking mode, the presence of octahedrally coordinated interlayer cations located above and/or below layer vacancies can give rise to three types of bonding between $H_2O_{interlayer}$ and the nearest O_{layer} from the adjacent layer. In the first [model 1a (polytype $1H$)], strong H-bonds link these species as they form empty prisms with short $H_2O_{interlayer}$-O_{layer} distances along the prism edges (2.70–2.75 Å—Fig. 3a). In the second [model 2a (polytype $3R_1$), model 3a (polytype $3R_2$), and model 4a (polytype $2H_1$)], O_{layer} and $H_2O_{interlayer}$ are linked by weak H-bonds as they form empty octahedra with long $H_2O_{interlayer}$-O_{layer} distances (3.0–3.15 Å—Fig. 3b). In the third interlayer type [model 5a (polytype $2H_2$), model 6a [polytype $3H_1$], and model 7a (polytype $3H_2$)], empty prisms and empty octahedra formed by O_{layer} and $H_2O_{interlayer}$ coexist within a given interlayer, with prisms located on one side of the interlayer and octahedra on the opposite one (Fig. 3c).

The presence of tetrahedrally coordinated interlayer cations located above and/or below the vacant layer octahedra in model 3b (polytype $3R_2$) is associated with the formation of strong H-bonds between $H_2O_{interlayer}$ coordinating the interlayer cations and nearest O_{layer} from the adjacent layer. Both species are superimposed in projection on the **a-b** plane and thus located close to each other (Fig. 3d). The coexistence of both octahedrally and tetrahedrally coordinated interlayer cations in model 5c (polytype $2H_2$) leads to the formation of empty prisms between the $H_2O_{interlayer}$ and O_{layer} (strong H-bonds) on one side of the interlayer and to short $H_2O_{interlayer}$-O_{layer} distances on the other side (not shown).

On the other hand, if birnessite interlayers contain large mono- or divalent cations, such as K^+, Ba^{2+}, Sr^{2+}, or Cs^+, then they will be located in the interlayer mid-plane either in octahedra defined by O_{layer} from adjacent layers [model 5b (polytype $2H_2$), and model 6b (polytype $3H_1$)] or in interlayer prisms [model 2b (polytype $3R_1$)]. In the latter case, interlayer prisms share one face with a layer octahedron and three edges with occupied octahedra of the adjacent layer. Local charge compensation is achieved when interlayer cations are distributed so that prisms share a face with vacant layer octahedra. Random distribution of interlayer cations leads to electrostatic repulsion with Mn_{layer} despite the presence of layer vacancies. Table 2 lists birnessite polytypes consisting of hexagonal vacancy-bearing layers that differ from each other by stacking modes and interlayer structures, which are reasonable from a crystal-chemical point of view.

Polytypes with orthogonal layer symmetry. The interlayer cations for vacancy-free layers should have sixfold coordination by O_{layer} and $H_2O_{interlayer}$, and be distributed so as to avoid direct interaction with Mn_{layer}. The $1O$, $2O_2$, $3O_1$, and $3O_2$ polytypes are thus not suitable to host large mono- or divalent cations as they cannot avoid such interactions. In contrast, the $1M_2$ and $2O_1$ polytypes can host these cations in the interlayer mid-plane, with octahedral [model 3e (polytype $1M_2$)], or prismatic [model 4c (polytype $2O_1$) and model 4e (polytype $2O_1$)] coordinations.

Model 2c (polytype $1M_1$) represents a special case as interlayer cations cannot be located in a' or b' sites because of the interaction with Mn_{layer}. However, smaller interlayer cations, such

TABLE 2. Symbolic notations of birnessite consisting of hexagonal (vacancy-bearing) and orthogonal (vacancy-free) layers and differing from each other by stacking modes and interlayer structures

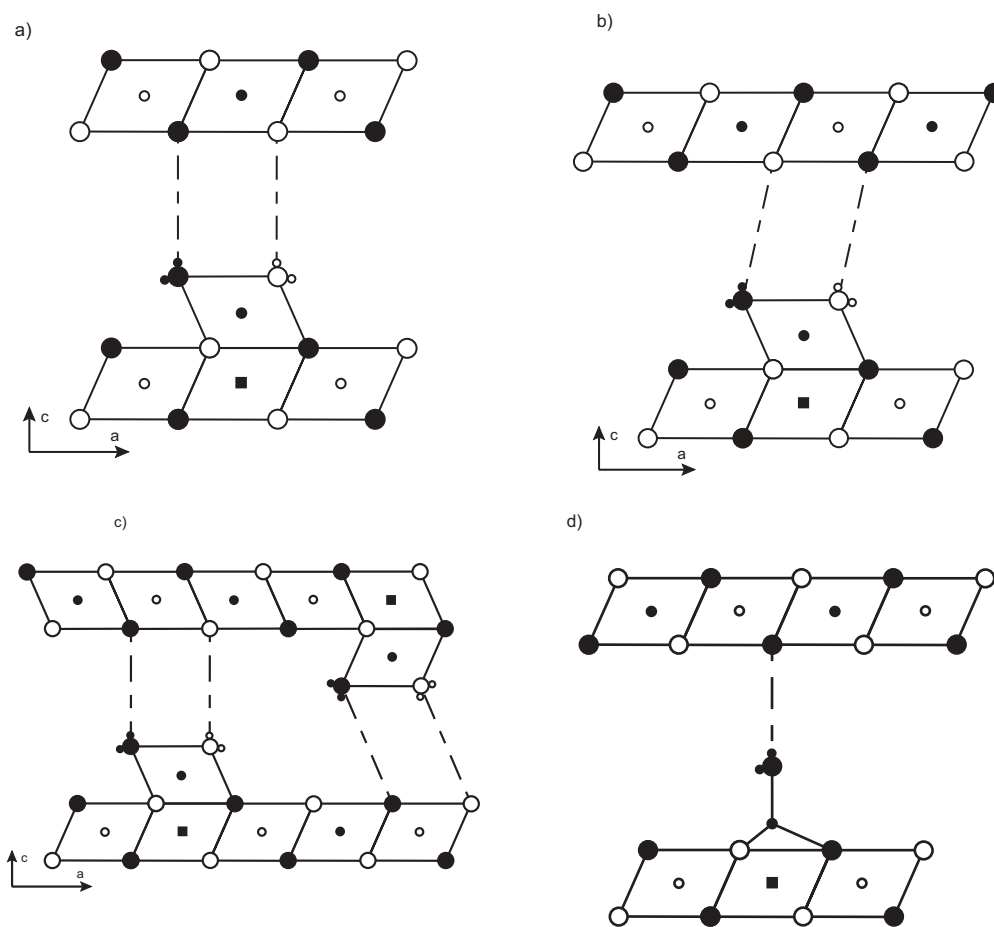| Hexagonal layer symmetry				Layers with orthogonal symmetry			
Polyt.	Model	XRD (Fig.)	Notation	Polyt.	Model	XRD (Fig.)	Notation
$1H$	1a	5a	$AbC_{b'A'},{}^{C'b'}AbC...$	$1O$	1b		$AbC_{a'B'},{}^{B'c'}AbC...$
$3R_1$	2a	5b, 8b	$AbC_{b'A'},{}^{B'a'}CaB_{a'C'},{}^{A'c'}BcA_{c'B'},{}^{C'b'}AbC...$	$1M_1$	2c		$AbC\ c'CaB\ b'BcA\ a'AbC...$
$3R_1$	2b	8a, 10a	$AbC\ b'/a'\ CaB\ a'/c'\ BcA\ c'/b'\ AbC...$		2d		$AbC_{a'A'},{}^{B'b'}CaB_{c'C'},{}^{A'a'}BcA_{b'B'},{}^{C'c'}AbC...$
$3R_2$	3a	6b, 10b	$AbC_{b'A'},{}^{A'c'}BcA_{c'C'},{}^{B'a'}CaB_{a'C'},{}^{C'b'}AbC...$	$1M_2$	3d	7b	$AbC_{a'B'},{}^{C'a'}BcA_{c'B'},{}^{A'b'}CaB_{c'A'},{}^{B'c'}AbC...$
$3R_2$	3b	5c, 6a	$AbC_{b'B'},{}^{C'c'}BcA_{c'C'},{}^{A'a'}CaB_{a'A'},{}^{B'b'}AbC...$	$1M_2$	3e	7a	$AbC\ a'BcA\ b'CaB\ c'AbC...$
$3R_2$	3c	6c	$AbC_{a'A'},{}^{A'a'}BcA_{b'B'},{}^{B'b'}CaB_{c'C'},{}^{C'c'}AbC...$	$2O_1$	4c	7c, 9c	$AbC\ a'CbA\ c'AbC...$
$2H_1$	4a	5d, 8d, 9b	$AbC_{b'A'},{}^{A'b'}CbA_{b'C'},{}^{C'b'}AbC...$	$2O_1$	4d	7d	$AbC_{a'B'},{}^{B'a'}CbA_{c'B'},{}^{B'c'}AbC...$
$2H_1$	4b	8c	$AbC\ a'/C'\ CbA\ c'/A'\ AbC...$	$2O_1$	4e		$AbC\ c'CbA\ a'AbC...$
		5e, 9a		$2O_2$	5d		$AbC_{a'B'},{}^{C'b'}AcB_{a'C'},{}^{B'c'}AbC...$
$2H_2$	5a		$AbC_{b'A'},{}^{B'c'}AcB_{c'A'},{}^{C'b'}AbC...$	$2O_2$	5e		$AbC_{a'A'},{}^{C'b'}AcB_{a'A'},{}^{B'c'}AbC...$
$2H_2$	5b		$AbC\ b'\ AcB\ c'\ AbC...$				
$2H_2$	5c		$AbC_{b'A'},{}^{C'c'}AcB_{c'A'},{}^{B'b'}AbC...$				
$3H_1$	6a	5f, 10c	$AbC_{b'A'},{}^{B'c'}AcB_{c'A'},{}^{B'c'}AcB_{c'A'},{}^{C'b'}AbC...$				
$3H_1$	6b	5g, 10d	$AbC\ b'AcB\ c'AcB\ c'AbC...$				
$3H_2$	7a		$AbC_{b'A'},{}^{B'c'}AcB_{c'A'},{}^{B'a'}CaB_{a'C'},{}^{C'b'}AbC...$				

FIGURE 3. Idealized interlayer structure model in projection along the **b** axis for birnessite polytypes with layer vacancies (hexagonal layer symmetry). Symbols and notations as in Figure 1. (**a**) $1H$ polytype with octahedrally coordinated cations above/below vacant layer sites (^{VI}TC position—Model 1a). Irregular dashed lines outline the interlayer prisms defined by $H_2O_{interlayer}$ coordinating the interlayer cations and O_{layer} from adjacent layers (H-bonds). (**b**) $3R_1$, $3R_2$, and $2H_1$ polytypes with octahedrally coordinated cations above/below vacant layer sites (^{VI}TC position—Models 2a, 3a, and 4a, respectively). Irregular dashed lines outline the interlayer octahedra defined by $H_2O_{interlayer}$ coordinating the interlayer cations and O_{layer} from adjacent layers (weak H-bonds). (**c**) $2H_2$, $3H_1$, and $3H_2$ polytypes with octahedrally coordinated cations above/below vacant layer sites (^{VI}TC position—Models 5a, 6a, and 7a, respectively). Irregular dashed lines outline the interlayer prisms (left) and octahedra defined by $H_2O_{interlayer}$ coordinating the interlayer cations and O_{layer} from adjacent layers (strong and weak H-bonds, respectively). (**d**) $3R_2$ polytype with tetrahedrally coordinated cations above/below vacant layer sites (^{IV}TC position—Model 3b). Irregular dashed line outlines the strong H-bond between $H_2O_{interlayer}$ coordinating the interlayer cation and O_{layer} from adjacent layers.

as Na^+, can be located, together with $H_2O_{interlayer}$, in the interlayer mid-plane above and/or below O_{layer} of adjacent layers as was described for Na-rich synthetic birnessite, hereafter referred to as NaBi (Lanson et al. 2002b). Similarly, in Na^+-saturated $2O_1$ polytype, the interlayer cations are likely located above and/or below O_{layer} from adjacent layers (model 4e).

Relatively small di- and trivalent interlayer cations may be located above and/or below empty layer tetrahedra (tridentate cavities) sharing three edges with layer Mn octahedra (^{VI}TE sites). Interlayer H_2O molecules provide octahedral coordination to these cations and may form either empty prisms [model 3d (polytype $1M_2$)—Fig. 4a] or empty octahedra [model 1b, (polytype $1O$), and model 4d (polytype $2O_1$)—Fig. 4b], with O_{layer} from the adjacent layer. Empty prisms and empty octahedra coexist within a given interlayer [model 5d (polytype $2O_2$)] if interlayer cations are octahedrally coordinated. If interlayer cations have both octahedral and tetrahedral coordination, then $H_2O_{interlayer}$ and O_{layer} in model 5e (polytype $2O_2$) form empty prisms and strong H-bonds on either side of a given interlayer. Table 2 lists birnessite polytypes consisting of orthogonal vacancy-free layers that differ from each other by stacking modes and interlayer structures, which are reasonable from a crystal-chemical point of view.

Vacancy-free birnessite layers can have hexagonal symmetry if the long Mn^{3+}-O bonds of the layer Mn^{3+}-octahedra are randomly oriented with respect to the **a** axis by n60° (Gaillot et al. 2005, 2007). Interlayer cations in such birnessite layers should be distributed so as to avoid direct interaction with the nearest Mn_{layer}. In this case, suitable interlayer structures are those described for vacancy-free orthogonal layers (Table 2).

CALCULATION OF XRD PATTERNS

The XRD patterns calculated for polytypes with the same layer symmetry and periodicity along the **c*** axis have the same *d*-spacings, but differ by their *hkl* intensity distributions. Characterization of layer silicates has shown that structures can be approximated by models for polytype identification purpose. The influence of the actual layer structure on the *hkl* intensity distributions is indeed a second-order effect compared to the differences among polytypes (Bailey 1980). Structure models were thus proposed for each birnessite variety and corresponding powder XRD patterns were calculated. All calculations were performed using the program developed by Plançon (2002) on the basis of the formalism described by Drits and Tchoubar (1990). No orientation function was considered, and no random stacking faults were introduced for the calculations.

Initial structure models

In all structure models, Mn_{layer} and O_{layer} occupy special sites in the orthogonal C-centered unit cell: (0, 0, 0), (0.333, 0, z), and (–0.333, 0, –z), respectively, where z-coordinates (in projection on the **c*** axis) were equal to 1.00 Å (Post and Veblen 1990; Drits et al. 1998; Lanson et al. 2000, 2002a, 2002b; Gaillot et al. 2003, 2005). According to the close-packing notation, interlayer cations and $H_2O_{interlayer}$ also occupy special sites. In the initial structure models, the z-coordinates of the interlayer cations (Me) and $H_2O_{interlayer}$ are the sole variable parameters. The initial z-coordinates of Me and H_2O molecules can be estimated from typical Me-O and Me-H_2O bond lengths for fourfold- and sixfold-coordinated Me and from elementary geometrical relationships between these bond lengths and corresponding z-coordinates. For example, if an interlayer cation is octahedrally coordinated above and/or below a vacant layer octahedron, then the following equations are deduced from the hexagonal symmetry of the layer (Lanson et al. 2002b):

$$z(Me) = z(O_{layer}) + \sqrt{d^2(Me-O) - \frac{b^2}{3}} = z(O_{layer}) + \Delta z$$

and

$$z(H_2O) = z(O_{layer}) + 2\Delta z.$$

In the present work, Me-O and Me-H_2O interatomic distances were determined from the effective ionic radii given by Shannon (1976). Where applicable, the interlayer atomic positions were adapted from published structural determination of synthetic Na-birnessite (Lanson et al. 2002a), Ca-birnessite (Drits et al. 1998), H-birnessite (Lanson et al. 2000), and K-birnessites (Gaillot et al. 2003, 2005). In the various structure models K, Ca, Mn, Na, and/or Mg were used as interlayer cations. For the different structure models presented in Table 2, corresponding atomic positions and their occupancies are listed in Table 3.

Calculated XRD patterns

Powder XRD patterns calculated for the different polytypes are shown in Figures 5–8, whereas *d*-values and *hkl* indices of reflections observed on the various patterns are listed in Table 4. Indexing is performed assuming an orthogonal C-centered cell for both hexagonal and orthogonal birnessite. Reflections in the 36–64 °2θ Cu$K\alpha$ range have 20*l*,11*l* indices (10*l* and 01*l* when using a hexagonal unit cell), whereas they have 31*l*,02*l* indices (11*l* when using a hexagonal unit

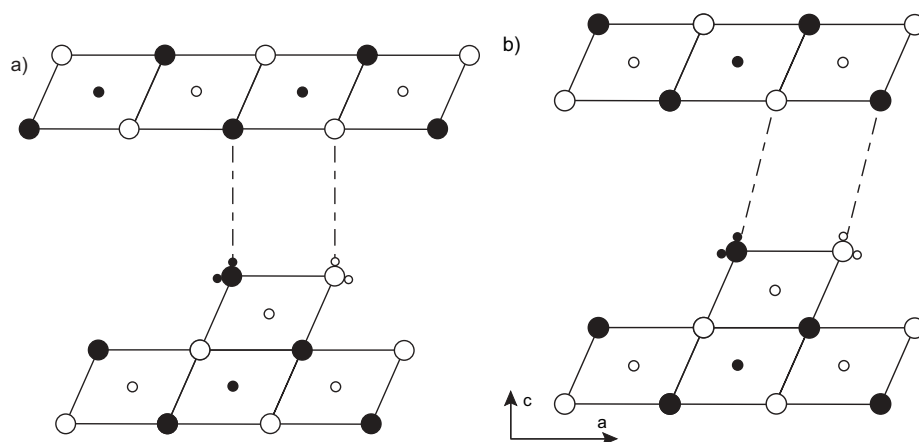**FIGURE 4.** Idealized interlayer structure model in projection along the **b** axis for birnessite polytypes with vacancy-free layers (orthogonal layer symmetry). (**a**) $1M_2$ polytype with octahedrally coordinated cations above/below empty layer tetrahedra (tridentate cavities) sharing three edges with layer Mn octahedra (^{VI}TE position—Model 3d). Symbols and notations as in Figure 1. Irregular dashed lines outline the interlayer prisms defined by $H_2O_{interlayer}$ coordinating the interlayer cations and O_{layer} from adjacent layers (H-bonds). (**b**) $1O$ and $2O_1$ polytypes with octahedrally coordinated cations above/below empty layer tetrahedra (tridentate cavities) sharing three edges with layer Mn octahedra (^{VI}TE position—Models 1b and 4d, respectively). Irregular dashed lines outline the interlayer octahedra defined by $H_2O_{interlayer}$ coordinating the interlayer cations and O_{layer} from adjacent layers (weak H-bonds).

TABLE 3. Atomic positions and site occupancies for the idealized structure models described in Table 2

Model		1a	2a	2b
Polytype		1*H*	3*R*₁	3*R*₁
XRD pattern	Fig.	5a	5b, 8b	8a
Mn_layer	x*	0	0	0
	y*	0	0	0
	ζ†	0	0	0
	Occ	0.833	0.833	0.925
O_layer	x*	+0.333/−0.333‡	+0.333/−0.333‡	+0.333/−0.333‡
	y*	0	0	0
	ζ†	+1.00/−1.00‡	+1.00/−1.00‡	+1.00/−1.00‡
	Occ	1 ×2	1 ×2	1 ×2
Cat. Inter.	Type	Mn	Mn	K
	x*	0.000	0.000	0
	y*	0	0	0
	ζ†	+2.15/−2.15‡	+2.15/−2.15‡	+3.55/−3.55‡
	Occ	0.0833 ×2	0.0833 ×2	0.15 ×2
H₂O	x*	−0.333/+0.333‡	−0.333/+0.333‡	−0.333/+0.333‡
	y*	0	0	0
	ζ†	+3.35/−3.35‡	+3.35/−3.35‡	+3.55/−3.55‡
	Occ	0.250 ×2	0.250 ×2	0.300 ×2
Interlayer shift		0.0	−0.333a	−0.333a

Model		3a	3b	3c	3d	3e
Polytype		3*R*₂	3*R*₂	3*R*₂	1*M*₂	1*M*₂
XRD pattern	Fig.	8b, 10b	5c, 6a	6c	7b	7a
Mn_layer	x*	0	0	0	0	0
	y*	0	0	0	0	0
	ζ†	0	0	0	0	0
	Occ	0.833	0.833	0.833	0.833	1.000
O_layer	x*	+0.333/−0.333‡	+0.333/−0.333‡	+0.333/−0.333‡	+0.333/−0.333‡	+0.333/−0.333‡
	y*	0	0	0	0	0
	ζ†	+1.00/−1.00‡	+1.00/−1.00‡	+1.00/−1.00‡	+1.00/−1.00‡	+1.00/−1.00‡
	Occ	2	2	2	2	2
Cat. Inter.	Type	Zn	Zn	Zn	Ca	K
	x*	0.000	0.000	−0.333/+0.333‡	−0.333/+0.333‡	−0.333/+0.333‡
	y*	0	0	0	0	0
	ζ†	+2.20/−2.20‡	+1.77/−1.77‡	+1.77/−1.77‡	+2.30/−2.30‡	+3.55/−3.55‡
	Occ	0.0833 ×2	0.0833 ×2	0.0833 ×2	0.0833 ×2	0.150 ×2
H₂O	x*	−0.333/+0.333‡	0	−0.333/+0.333‡	0	−0.333/+0.333‡
	y*	0	0	0	0	0
	ζ†	+3.55/−3.55‡	+3.70/−3.70‡	+3.70/−3.70‡	+3.70/−3.70‡	+3.55/−3.55‡
	Occ	0.250 ×2	0.0833 ×2	0.0833 ×2	0.250 ×2	0.300 ×2
Int. shift		+0.333a	+0.333a	+0.333a	+0.333a	+0.333a

TABLE 3.—*Continued*

Model		4a	4b	4c	4d	5a
Polytype		2*H*₁	2*H*₁	2*O*₁	2*O*₁	2*H*₂
XRD pattern	Fig.	5d, 8d, 9b, 10d	8c	7c	7d	5e, 9a
Mn_layer	x*	0	0	0	0	0
	y*	0	0	0	0	0
	ζ†	0	0	0	0	0
	Occ	0.833	0.925	1.000	1.000	0.833
O_layer	x*	+0.333/−0.333‡	+0.333/−0.333‡	+0.333/−0.333‡	+0.333/−0.333‡	+0.333/−0.333‡
	y*	0	0	0	0	0
	ζ†	+1.00/−1.00‡	+1.00/−1.00‡	+1.00/−1.00‡	+1.00/−1.00‡	+1.00/−1.00‡
	Occ	2	2	2	2	2
Cat. Inter.	Type	Mn	K	K	Ca	Mn
	x*	0.000	−0.222, 0.111/0.111	−0.222, 0.111/0.111	−0.333/+0.333‡	0
	y*	0	0, +0.333/−0.333‡	0, +0.333/−0.333‡	0	0
	ζ†	+2.15/−2.15‡	3.55	3.55	+2.30/−2.30‡	+2.15/−2.15‡
	Occ	0.0833 ×2	0.100 ×3	0.100 ×3	0.0833 ×2	0.0833 ×2
H₂O	x*	−0.333/+0.333‡	0.333	0.333	0	−0.333/+0.333‡
	y*	0	0	0	0	0
	ζ†	+3.35/−3.35‡	+3.55‡	+3.55‡	+3.70/−3.70‡	+3.35/−3.35‡
	Occ	0.250 ×2	0.600	0.600	0.250 ×2	0.250 ×2
Mn_layer	x*	0	0	0	0	0.333
	y*	0	0	0	0	0
	ζ†	7.10	7.10	7.10	7.10	7.10
	Occ	0.833	0.925	1.000	1.000	0.833
O_layer	x*	+0.333/−0.333‡	+0.333/−0.333‡	+0.333/−0.333‡	+0.333/−0.333‡	−0.333/0.000‡
	y*	0	0	0	0	0
	ζ†	6.10/8.10‡	6.10/8.10‡	6.10/8.10‡	6.10/8.10‡	6.10/8.10‡
	Occ	2	2	2	2	2
Cat. Inter.	Type	Mn	K	K	Ca	Mn
	x*	0.000	0.222, −0.111/−0.111‡	0.222, −0.111/−0.111‡	−0.333/+0.333‡	0.333
	y*	0	0, +0.333/−0.333‡	0, +0.333/−0.333‡	0	0
	ζ†	4.95/9.25‡	10.65	10.65	4.80/9.40‡	4.95/9.25‡
	Occ	0.0833 ×2	0.100 ×3	0.100 ×3	0.0833 ×2	0.0833 ×2
H₂O	x*	−0.333/+0.333‡	−0.333	−0.333	0	0.000/−0.333‡
	y*	0	0	0	0	0
	ζ†	3.75/10.45‡	10.65	10.65	3.40/10.80‡	3.75/10.45‡
	Occ	0.250 ×2	0.600	0.600	0.250 ×2	0.250 ×2
Int. shift		0	0	0	0	0

Note: Occupancy (Occ) is given as the sum of all equivalent sites.
* x and y atomic positions are expressed in fraction of ideal C-centered unit-cell *a* and *b* parameters, respectively. The x positions are given in projection normal to the **a-b** plane.
† Position ζ along *c* is expressed in angstroms to emphasize the thickness of layer and interlayer polyhedra.
‡ When multiple positions are listed for a given species, coordinates are all listed in the same order. Coordinates of related species (e.g., H₂O molecules coordinating cations) are also listed in the same order for a given structure model.

cell) over the 64–75 °2θ CuKα range. The XRD patterns shown in Figure 5 correspond to structure models in which interlayer Mn cations are located above and/or below layer sites and are octahedrally coordinated by O_layer and H₂O_interlayer (^VITC sites—Table 3). The calculated XRD patterns (Fig. 5) can be used to identify vacancy-bearing birnessite having one-, two-, and three-layer periodicity along the **c** axis and different layer stacking. However, analysis of the XRD patterns calculated for a given birnessite polytype having different interlayer structures shows that, for a given birnessite polytype, the intensity of *hkl* reflections also depends on the chemical nature of interlayer cations, their distribution, and local environment. For example, interlayer spaces of 3*R*₂ polytype (models 3a and 3b) may be occupied by Zn cations having octahedral and/or tetrahedral coordination (Manceau et al. 2000c; Lanson et al. 2000, 2002a) and located in TC sites or TE sites. The replacement of tetrahedrally for octahedrally coordinated Zn cations leads to a significant decrease of 204/114, 208/118, and 20.10/11.10 peak intensity (104, 018, and 10.10 assuming a hexagonal cell), with respect to the strongest 20*l*/11*l* reflections (Figs. 6a and 6b). Location of Zn cations in ^IVTE sites [model 3c (polytype 3*R*₂)—Fig. 6c] strongly increases the 204/114 and 207/117 reflection intensities, with respect to 201/111. Important redistribution of intensities is observed also for the 2*O*₁ and 1*M*₂ polytypes when interlayers are occupied either by large K⁺ (models 4c and 3e) or by smaller Ca²⁺ (models 4d and 3d). The transition from model 3e to model 3d significantly increases 201, 110, 112, 203, and 11̄2, and decreases the 111 and 113 intensities (Figs. 7a and 7b). Similarly, the transition from model 4c to 4d is accompanied by redistribution of the 112 and 114 maxima: strong

112 and moderate 114 peaks for model 4c are replaced by strong 114 and moderate 112 ones for model 4d (Figs. 7c and 7d).

In contrast, the relative intensity of strong, moderate, and weak reflections change very little for the 3*R*₁ polytype when interlayers are occupied by either K⁺, Ca²⁺, or Mn³⁺. The only significant change in the MnBi XRD pattern compared to KBi is a strong increase of 201/111 intensity (Figs. 8a and 8b). For the 2*H*₁ polytype, a strong increase of 200 and 203 intensities and a limited increase of the 206 one is visible on the XRD pattern calculated for MnBi model compared to KBi (models 4a and 4b—Figs. 8c and 8d).

The calculated XRD patterns show the limited influence of the interlayer structure on the *hkl* intensity distribution for a given birnessite polytype. The

TABLE 3.—*Continued*

Model		6a	7a
Polytype		$3H_1$	$3H_2$
XRD pattern	Fig.	5f, 10c	5g
Mn$_{layer}$	x*	0	0
	y*	0	0
	ζ†	0	0
	Occ	0.833	0.833
O$_{layer}$	x*	+0.333/–0.333‡	+0.333/–0.333‡
	y*	0	0
	ζ†	+1.00/–1.00‡	+1.00/–1.00‡
	Occ	2	2
Cat. Inter.	Type	Mn	Mn
	x*	0	0
	y*	0	0
	ζ†	+2.15/–2.15‡	+2.15/–2.15‡
	Occ	0.0833 ×2	0.0833 ×2
H$_2$O	x*	–0.333/+0.333‡	–0.333/+0.333‡
	y*	0	0
	ζ†	+3.35/–3.35‡	+3.35/–3.35‡
	Occ	0.250 ×2	0.250 ×2
Mn$_{layer}$	x*	0.333	0.333
	y*	0	0
	ζ†	7.10	7.10
	Occ	0.833	0.833
O$_{layer}$	x*	–0.333/0.000‡	–0.333/0.000‡
	y*	0	0
	ζ†	6.10/8.10‡	6.10/8.10‡
	Occ	2	2
Cat. Inter.	Type	Mn	Mn
	x*	0.333	0.333
	y*	0	0
	ζ†	4.95/9.25‡	4.95/9.25‡
	Occ	0.0833 ×2	0.0833 ×2
H$_2$O	x*	0.000/–0.333‡	0.000/–0.333‡
	y*	0	0
	ζ†	3.75/10.45‡	3.75/10.45‡
	Occ	0.250 ×2	0.250 ×2
Mn$_{layer}$	x*	0.333	–0.333
	y*	0	0
	ζ†	14.20	14.20
	Occ	0.833	0.833
O$_{layer}$	x*	–0.333/0.000‡	0.333/0.000‡
	y*	0	0
	ζ†	13.20/15.20‡	13.20/15.20‡
	Occ	2	2
Cat. Inter.	Type	Mn	Mn
	x*	0.333	–0.333
	y*	0	0
	ζ†	12.05/16.35‡	12.05/16.35‡
	Occ	0.0833 ×2	0.0833 ×2
H$_2$O	x*	0.000/–0.333‡	0.000/0.333‡
	y*	0	0
	ζ†	10.85/17.55‡	10.85/17.55‡
	Occ	0.250 ×2	0.250 ×2
Int. shift		0	0

Note: Occupancy (Occ) is given as the sum of all equivalent sites.
* x and y atomic positions are expressed in fraction of ideal C-centered unit-cell *a* and *b* parameters, respectively. The x positions are given in projection normal to the **a-b** plane.
† Position ζ along *c* is expressed in angstroms to emphasize the thickness of layer and interlayer polyhedra.
‡ When multiple positions are listed for a given species, coordinates are all listed in the same order. Coordinates of related species (e.g., H$_2$O molecules coordinating cations) are also listed in the same order for a given structure model.

intensity distribution is primarily determined by the polytype (Figs. 6–8). As a consequence, identification of birnessite polytypes having either hexagonal or C-centered orthogonal ($a > b\sqrt{3}$) unit cells may be performed without a priori details of their layer and interlayer structures.

DISCUSSION

Criteria for determination of birnessite polytypes

Birnessite polytypes having the same periodicity along the **c** axis, but with different layer symmetry, differ from each other

TABLE 4A. Calculated *d(hkl)* values for birnessite polytypes consisting of vacancy-bearing layers having a hexagonal layer symmetry (See Table 1)

Polytype	1H	2H	3R/3H
d(hkl)	hkl	hkl	hkl
2.468	200,110	200,110	200,110
2.452	–	–	201,111
2.432	–	201,111	–
2.404	–	–	202,112
2.331	201,111	202,112	203,113
2.239	–	–	204,114
2.188	–	203,113	–
2.136	–	–	205,115
2.026	202,112	204,114	206,116
1.917	–	–	207,117
1.863	–	205,115	–
1.810	–	–	208,118
1.708	203,113	206,116	209,119
1.613	–	–	20.10,11.10
1.567	–	207,117	–
1.523	–	–	20.11,11.11
1.441	204,114	208,118	20.12,11.12
1.425	020,310	020,310	020,310
1.422	–	–	021,311
1.418	–	021,311	–
1.412	–	–	022,312
1.397	021,311	022,312	023,313
1.376	–	–	024,314
1.365	–	–	20.13,11.13
1.364	–	023,313	–
1.351	–	–	025,315
1.329	–	209,119	–
1.322	022,312	024,314	026,316
1.295	–	–	20.14, 11.14
1.290	–	–	027,317
1.274	–	025,315	–
1.256	–	–	028,318
1.231	–	20.10,11.10	20.15,11.15
1.221	023,313	026,316	029,319

Notes: a and *b* unit-cell parameters are 4.936 and 2.850 Å, respectively. The minimum periodicity along the **c*** axis is 7.10 Å for all polytypes.

by the number of *hkl* reflections. For example, the hexagonal birnessite exhibits a single series of 20*l*/11*l* reflections, whereas 20*l* and 11*l* series of reflections are individualized for birnessite with an orthogonal layer symmetry. In addition, XRD patterns of hexagonal birnessite usually contain a diagnostic 310/020 reflection (110 when using the hexagonal cell) with $d = 1.42 \pm 0.01$ Å, whereas for the orthogonal birnessite this reflection is split with $d(310) > d(020) = 1.42 \pm 0.01$ Å.

Birnessites with similar periodicity and layer symmetry can be differentiated by the intensity distribution of *hkl* reflections. Figures 9a and 9b show that *hkl* reflections with $l = 2n$ are more intense for $2H_1$ polytype compared to those of $2H_2$ polytype. In contrast, 20*l*/11*l* reflections (10*l* and 01*l* when using the hexagonal cell) with $l = 2n + 1$ are significantly stronger for $2H_2$ polytype. Similarly, 11*l* and 20*l* reflections with $l = 2n$ are stronger than those with $l = 2n +1$ for the $2O_1$ polytype (Fig. 9c). XRD patterns from $3R_1$ and $3R_2$ polytypes also differ from each other by their intensity distributions among *hkl* reflections. The 20*l*/11*l* reflections with $l = 3n – 1$ (01*l* with $l = 3n – 1$ ones if using the hexagonal cell) are intense for $3R_1$ polytype but not for $3R_2$, whereas 20*l*/11*l* reflections with $l = 3n + 1$ (10*l* with $l = 3n + 1$ ones if using the hexagonal cell) are intense for $3R_2$ polytype and weak for $3R_1$ (Figs. 10a and 10b). $3H_1$ and $3H_2$ polytypes differ from $3R_1$ and $3R_2$ by the presence of 20*l*/11*l* reflections with $l = 3n$ (Figs 10c and 10d). Similarly, intensity of 20*l*/11*l* reflections with $l = 3n$ (10*l* with $l = 3n$ if using the hexagonal cell) is significantly lower for

TABLE 4B. Calculated $d(hkl)$ values for birnessite polytypes consisting of vacancy-free layers having an orthogonal layer symmetry (See Table 1)

Polytype $d(hkl)$	1O hkl	1M_1 hkl	1M_2 hkl	2O_1/2O_2 hkl
2.590	200			200
2.571		20$\overline{1}$	201	
2.548				201/20$\overline{1}$
2.517		200	200	
2.497	110			110
2.480		110	110	
2.459				111/11$\overline{1}$
2.433	201/20$\overline{1}$			202/20$\overline{2}$
2.431		11$\overline{1}$	111	
2.356	111/11$\overline{1}$			112/11$\overline{2}$
2.329		20$\overline{2}$	202	
2.272				203/20$\overline{3}$
2.261		111	11$\overline{1}$	
2.214		201	201	
2.209				113/11$\overline{3}$
2.154		11$\overline{2}$	112	
2.092	202/20$\overline{2}$			204/20$\overline{4}$
2.042	112/11$\overline{2}$			114/11$\overline{4}$
1.972		20$\overline{3}$	203	
1.930		112	11$\overline{2}$	
1.914				205/20$\overline{5}$
1.875				115/11$\overline{5}$
1.857		20$\overline{2}$	202	
1.821		113	113	
1.747	203/20$\overline{3}$			206/20$\overline{6}$
1.718	113/11$\overline{3}$			116/11$\overline{6}$
1.645		20$\overline{4}$	204	
1.621		113	11$\overline{3}$	
1.597				207/20$\overline{7}$
1.574				117/11$\overline{7}$
1.551		20$\overline{3}$	203	
1.530		11$\overline{4}$	114	
1.477	310	311	311	310
1.469				311/31$\overline{1}$
1.464	204/20$\overline{4}$			208/20$\overline{8}$
1.447	114/11$\overline{4}$			118/11$\overline{8}$
1.446	311/31$\overline{1}$	310/31$\overline{2}$	310/312	312/31$\overline{2}$
1.425	020	020	020	020
1.418				021/02$\overline{1}$
1.410				313/31$\overline{3}$
1.397	021/02$\overline{1}$	021/02$\overline{1}$	021/021	022/02$\overline{2}$
1.384		205	205	
1.370		114	114	
1.365				023/02$\overline{3}$
1.364	312/31$\overline{2}$	31$\overline{1}$	31$\overline{1}$	314/31$\overline{4}$
1.363		313	313	
1.347				209/20$\overline{9}$
1.334				119/11$\overline{9}$
1.322	022/02$\overline{2}$	022/02$\overline{2}$	022/02$\overline{2}$	024/02$\overline{4}$
1.312		204	204	
1.310				315/31$\overline{5}$
1.299		11$\overline{5}$	115	
1.274				025/02$\overline{5}$
1.253	313/31$\overline{3}$	312/31$\overline{4}$	314/31$\overline{2}$	316/31$\overline{6}$
1.245	205/20$\overline{5}$			20.10/20.$\overline{10}$
1.234	115/11$\overline{5}$			11.10/11.$\overline{10}$
1.221	023/02$\overline{3}$	023/02$\overline{3}$	023/02$\overline{3}$	026/02$\overline{6}$

Notes: a and *b* unit–cell parameters are 5.180 and 2.850 Å, respectively. The minimum periodicity along the **c*** axis is 7.10 Å for all polytypes. The β angle is 103.65 and 76.35° for 1M_1 and 1M_2 polytypes, respectively.

3H_2 than for 3H_1 (Figs. 10c and 10d). The intensity distribution among *hkl* reflections described above for 3R_1, 3R_2, 3H_1, and 3H_2 polytypes remain valid for the equivalent birnessite polytypes with orthogonal layer symmetry (1M_1, 1M_2, 3O_1, 3O_2).

Special attention should be paid to identify one- (1H and 1O) and two-layer (2H_1 and 2O_1) polytypes having the same layer symmetry. The presence of a weak 203/113 reflection is the sole distinguishing feature, allowing identification of the two-layer polytypes (Figs. 5a and 5b). Note that the difference between

XRD patterns corresponding to these two polytypes is further reduced when 1H layer pairs are present in the 2H_1 polytype (that is when AbC – AbC pairs are present in crystals dominated by AbC = CbA = AbC... sequences) as the intensity of the 203/113 reflection is significantly decreased by the presence of such 1H layer pairs in a mixed-layered structure (not shown).

Stacking faults

The above-described method can be used not only for the identification of birnessite polytypes but also to determine the nature of stacking faults that are typically present in natural and synthetic birnessites. Well-defined and random stacking faults significantly alter XRD patterns from defective layer structures (for definition of well-defined and random stacking faults, see Drits and Tchoubar 1990). Well-defined stacking faults correspond to the interstratification of layer pairs having the same thickness but different internal structure and interlayer displacements within a periodic polytype. As the result of such interstratification, *hkl* reflections are shifted, and their positions become irrational.

Drits and McCarty (1996) have shown that Méring's rules, initially proposed for basal reflections (Méring 1949), can be generalized to account for the behavior of *hkl* reflections from defective layer structures. According to these generalized rules, *hkl* reflections observed from a defective layer structure are located between neighboring *hkl* reflections of periodic phases whose fragments (layer pairs in the present case) are interstratified. The actual position of *hkl* reflections corresponding to the defective layer structure depends on the relative proportion of the structure fragments and on relative intensities of the "involved" *hkl* reflections of the periodic phases.

For example, Lanson et al. (2002b—Fig. 3) showed that reflections of Zn-sorbed birnessite are located between *hkl* reflections calculated for 3R_2 and 1H polytypes and hypothesized that the main 3R_2 polytype contained some 1H layer pairs (i.e., AbC – AbC pairs are present in crystals dominated by AbC – BcA – CaB – AbC... sequences). As a result, positions of *hkl* reflections of the main 3R_2 polytype should indeed be shifted from their ideal position toward those of the defect-free 1H polytype. Accordingly, the best agreement between experimental and calculated XRD patterns was obtained for a defective 3R_2 polytype containing 12% of 1H layer pairs (Lanson et al. 2002b). A similar approach may be applied to mixtures containing periodic and defective birnessites. For example, Figure 11 shows the best possible agreement between an experimental XRD pattern and that calculated for a mixture of four birnessites: a periodic 2H_1 polytype and three defective ones (2O_1/2H_1, 2H_1/3R_1, and 3R_1/2H_1). In the three mixed-layered structures, layer pairs of the 2H_1 polytype are randomly interstratified with those of the 2O_1 and 3R_1 polytypes in proportions 1:1, 7:3, and 1:9, respectively. Note on Figure 11 that each of these mixed-layered structures gives a diagnostic contribution to the calculated XRD pattern (Gaillot et al. 2004).

In our experience, one of the most effective ways to study defective birnessite is to combine the above rules for polytype identification and interstratification to build up starting models for XRD pattern calculation (Manceau et al. 1997; Drits et al. 1998; Lanson et al. 2000, 2002a, 2002b; Gaillot et al. 2003, 2004,
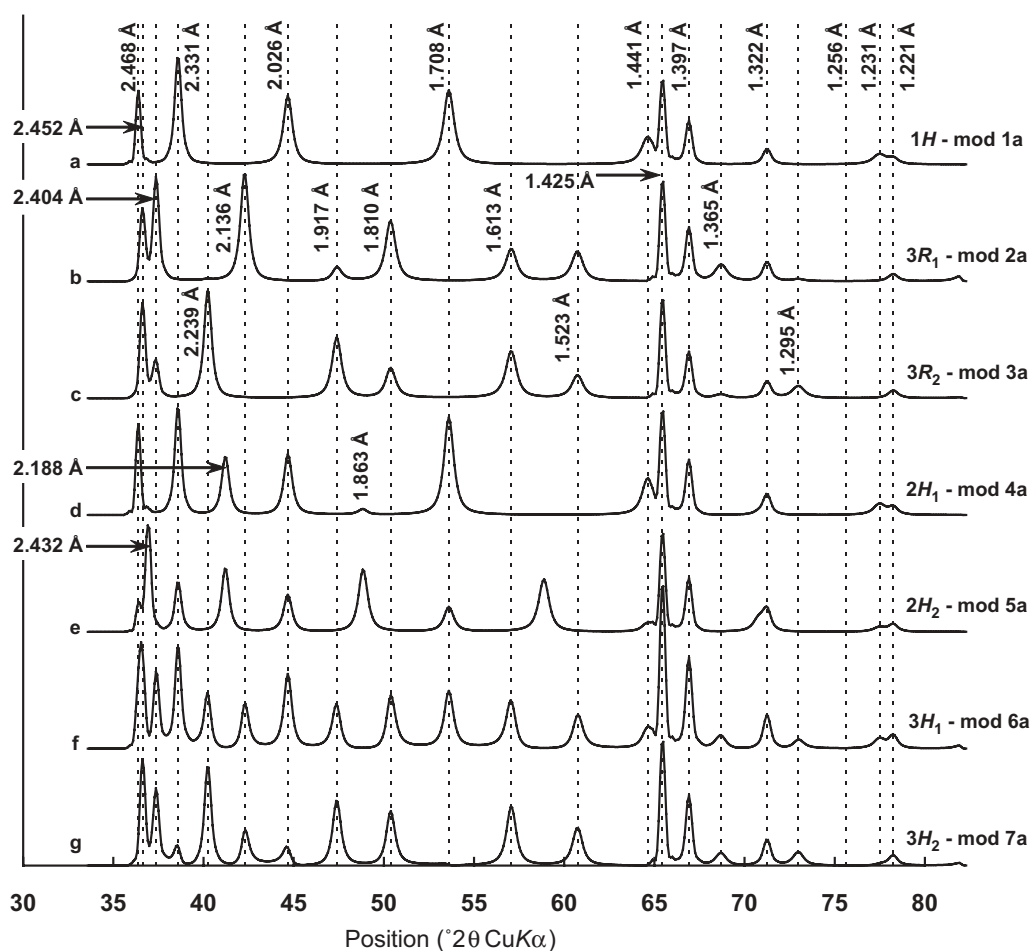
FIGURE 5. XRD patterns calculated for idealized structure models of birnessite polytypes. (**a**) $1H$ polytype with $Mn^{3+,2+}$ in ^{VI}TC position (Model 1a). (**b**) $3R_1$ polytype with $Mn^{3+,2+}$ in ^{VI}TC position (Model 2a). (**c**) $3R_2$ polytype with Zn^{2+} in ^{VI}TC position (Model 3a). (**d**) $2H_1$ polytype with $Mn^{3+,2+}$ in ^{VI}TC position (Model 4a). (**e**) $2H_2$ polytype with $Mn^{3+,2+}$ in ^{VI}TC position (Model 5a). (**f**) $3H_1$ polytype with $Mn^{3+,2+}$ in ^{VI}TC position (Model 6a). (**g**) $3H_2$ polytype with $Mn^{3+,2+}$ in ^{VI}TC position (Model 7a).

XRD patterns were calculated using the idealized structure models described in Table 3. a and b unit-cell parameters for the polytypes having a hexagonal layer symmetry are 4.936 and 2.850 Å, respectively, whereas they are 5.180 and 2.850 Å, for the polytypes having a orthogonal layer symmetry. In all cases the minimum periodicity along the $\mathbf{c}^*$ axis is 7.10 Å. All calculations were performed assuming a periodic stacking mode devoid of random stacking faults. The radius of the coherent scattering domains in the **a-b** plane was set to 150 Å for all calculations, whereas the mean extent of the coherent scattering domains perpendicular to the layer plane is 7 layers (maximum extent: 35 layers). The distribution of coherent scattering domain size along the $\mathbf{c}^*$ axis was assumed to be lognormal (Drits et al. 1997b). The values of Debye-Waller thermal factor (B) were 0.5, 1.0, and 1.5 for Mn_{layer}, O_{layer}, and $H_2O_{interlayer}$, respectively. B factors for $Me_{interlayer}$ were either 1.0 (metal cations Zn^{2+}, $Mn^{3+,2+}$ ...) or 2.0 (alkali and alkali-earth cations: K^+, Ca^{2+} ...).

2005). Defective birnessite may contain layer pairs, which were not reported so far for natural and synthetic periodic birnessite. Therefore, all theoretically possible birnessite polytypes should be considered to determine the nature of stacking faults by comparing experimental and calculated XRD patterns.

Birnessite polytypes reported for natural and synthetic birnessites

1H Polytype. The first detailed structural study of natural birnessite was performed by Chukhrov et al. (1985) on monomineralic birnessite micronodules dredged from the oceanic floor. The sample has a one-layer hexagonal unit cell and its structure corresponds to the $1H$ polytype (model 1a) in which interlayer Mn^{3+} and Mg^{2+} cations are octahedrally coordinated above and/or

below vacant layer octahedra. Ca^{2+} and Na^+ cations were also present in the interlayer. This structure model was further supported by X-ray absorption spectroscopy data (Manceau et al. 1992a, 1992b). Analysis of published experimental XRD patterns shows that $1H$ birnessite dominates in Mn-nodules from ocean and lake floors (Burns and Burns 1977; Drits et al. 1985). This $1H$ polytype occurs also in soil birnessite (Glover 1977).

Birnessite resulting from the equilibration at low pH of NaBi (obtained according to the Giovanoli protocol—Giovanoli et al. 1970b) was studied by Silvester et al. (1997), Drits et al. (1997a), and in more detail by Lanson et al. (2000). This proton-rich birnessite, hereafter referred to as HBi, has a one-layer hexagonal unit cell and a structure similar to model 1a. HBi can thus be considered a synthetic analog of natural $1H$ birnessite.
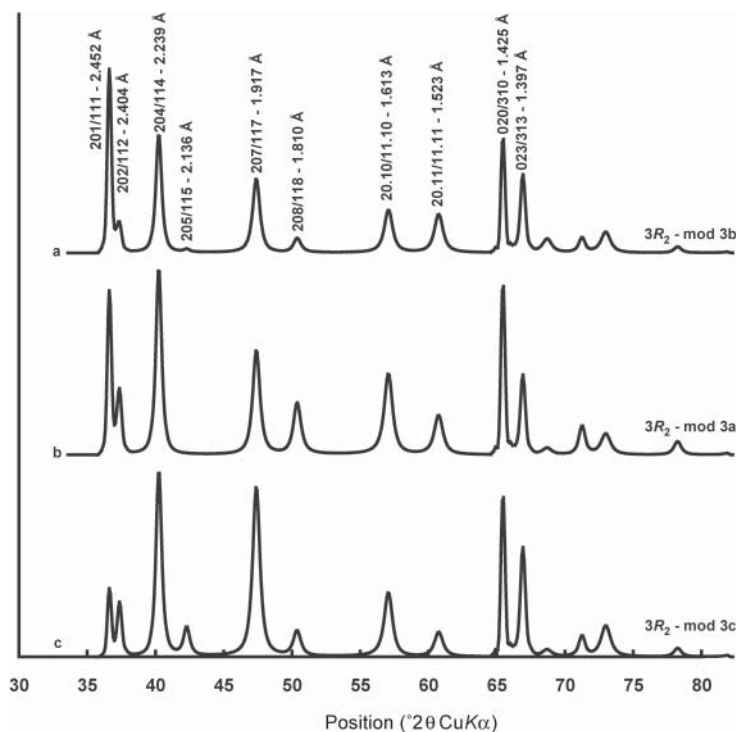
FIGURE 6. XRD patterns calculated for idealized structure models of birnessite $3R_2$ polytype. (**a**) With Zn^{2+} in ^{IV}TC position (Model 3b). (**b**) With Zn^{2+} in ^{VI}TC position (Model 3a). (**c**) With Zn^{2+} in ^{IV}TE position (Model 3c).

As natural $1H$ birnessite, HBi layers contain a significant amount of vacant layer octahedra capped by Mn^{2+} and Mn^{3+}. The negative layer charge of HBi is compensated for by protons and interlayer Mn cations, and the distribution of layer vacancies is inherited from the ordered Mn^{3+} distribution in NaBi. Interlayer H_2O molecules provide octahedral coordination to $Mn_{interlayer}$ and forms empty prisms, and strong H-bonds, with O_{layer} of the adjacent layer. Manceau et al. (1997) and Lanson et al. (2002b) showed that equilibration of NaBi in the presence of aqueous heavy metals (Co, Cd, and Pb) leads also to the formation of the $1H$ polytype (model 1a). When Zn^{2+} is present, the resulting Zn-sorbed synthetic birnessite (ZnBi) has a $3R_2$ polytype, in which models 3a and 3b coexist. Interlayer Zn^{2+} cations are systematically located above and/or below vacant layer sites but can have both octahedral and tetrahedral coordination. As a result, $H_2O_{interlayer}$ providing octahedral (model 3a) and tetrahedral (model 3b) coordination of Zn form weak and strong H-bonds, respectively, with O_{layer} of the adjacent layer.

$1M_1$ Polytype. Na-rich birnessite synthesized at high pH (Giovanoli et al. 1970a) was first described by Post and Veblen (1990) as a one-layer monoclinic polytype ($1M_1$ polytype, model 2c). To refine the structure, they used a $C2/m$ space group and the Rietveld technique. However, their results were not precise enough to draw definitive conclusions on the origin of the layer charge. Lanson et al. (2002a) showed that NaBi has a one-layer triclinic unit cell ($C\bar{1}$ space group) and consists of vacancy-free layers, the layer negative charge arising from the Mn^{3+}-for-Mn^{4+} substitution within octahedral layers. The orthogonal layer symmetry results from the Jahn-Teller distortion of Mn^{3+}-octahedra which all have their long Mn^{3+}-O_{layer} bond oriented along the **a** axis. Structural sites of interlayer Na and H_2O, and their occupancies, have also been determined. The triclinic
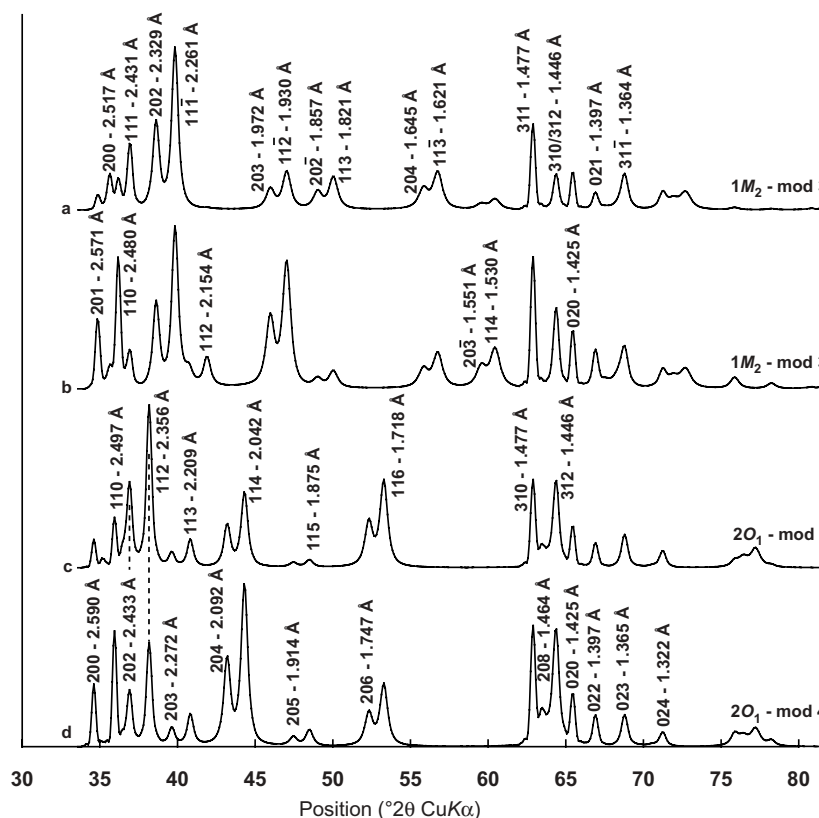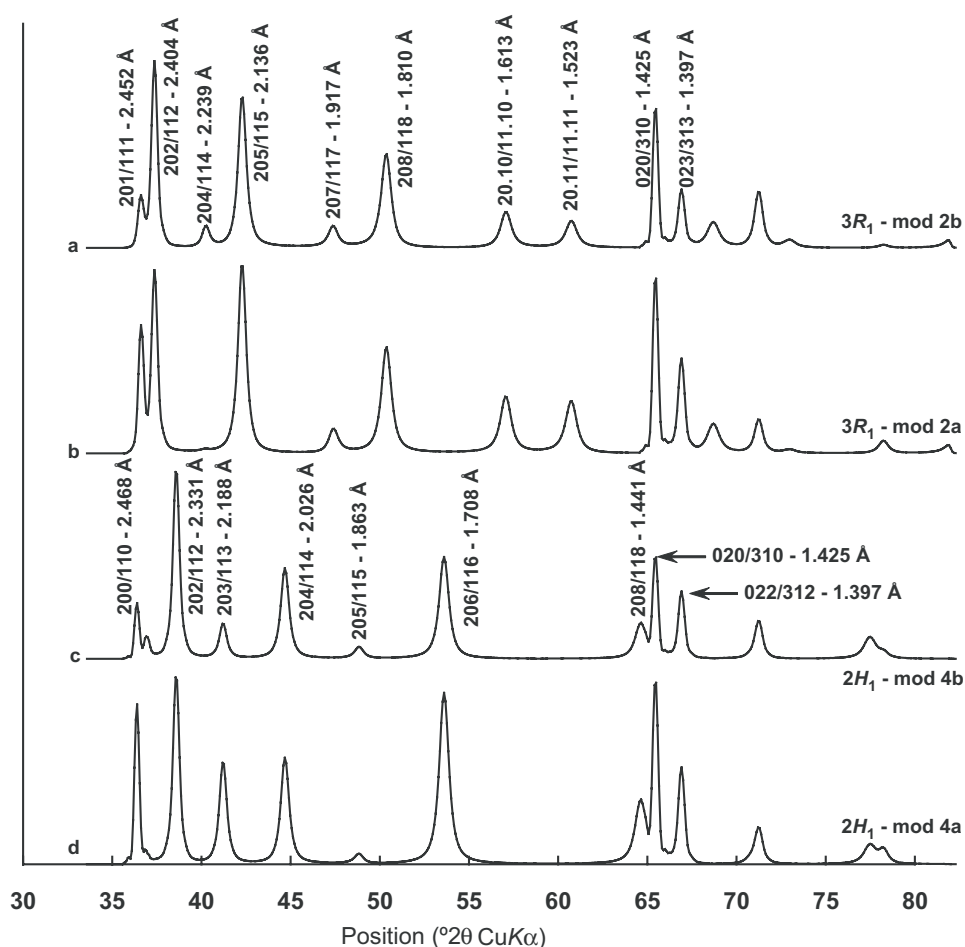

FIGURE 7. XRD patterns calculated for idealized structure models of birnessite polytypes. (**a**) $1M_2$ polytype with K^+ in the interlayer mid-plane (Model 3e). (**b**) $1M_2$ polytype with Ca^{2+} in ^{VI}TE sites (Model 3d). (**c**) $2O_1$ polytype with K^+ in the interlayer mid-plane (Model 4c). (**d**) $2O_1$ polytype with Ca^{2+} in ^{VI}TE sites (Model 4d).

FIGURE 8. XRD patterns calculated for idealized structure models of birnessite polytypes. (**a**) $3R_1$ polytype with K^+ in the interlayer mid-plane (Model 2b). (**b**) $3R_1$ polytype with $Mn^{3+,2+}$ in ^{VI}TC position (Model 2a). (**c**) $2H_1$ polytype with K^+ in the interlayer mid-plane (Model 4b). (**d**) $2H_1$ polytype with $Mn^{3+,2+}$ in ^{VI}TC position (Model 4a).

character of NaBi originates from a small layer displacement along the **b** axis.

NaBi varieties with different monovalent and divalent cations that were exchanged for Na^+ were studied by Post and Veblen (1990), Kuma et al. (1994), and Bartoli (1997). XRD patterns of these different birnessites can be indexed with a one-layer monoclinic unit cell whose parameters depend on the interlayer cation. However, essential details of these birnessites remain poorly understood. For example, Mg^{2+} cations in Mg-exchanged birnessite (MgBi) are supposedly located almost above or below octahedral sites (Post and Veblen 1990). Such a location is possible for interlayer Mg^{2+} cations only if the underlying octahedral sites are vacant, NaBi layers being vacancy-free.

Similarly, Bartoli (1997) reported in K-exchanged birnessite the location of K^+ cations in either a' or b' sites, whereas the presence of K^+ cations in these sites would lead to their direct interaction with Mn_{layer} from adjacent layers, as can be seen from symbolic notations (Model 2c—Table 2). Post and Veblen (1990) reported K^+ positions in KBi that are shifted from the center of the interlayer prism toward its edges.

Ca^{2+}-for-Na^+ exchange in NaBi dramatically modifies the initial one-layer triclinic structure of NaBi (model 2c) leading

to a four-layer polytype in which layer pairs having orthogonal stacking are shifted alternately by $\pm b/2$ along the **b** axis (Drits et al. 1998). Gorshkov et al. (1992) described an occurrence of natural Ca-bearing birnessite, which was analogous to the synthetic Ca-exchanged variety of NaBi.

$3R_1$ Polytype. Chen et al. (1996b) synthesized K-rich birnessite (KBi) with a $3R_1$ unit cell (model 2b). The KBi layers contain only Mn^{4+} and vacancies. From the refinement of integrated intensities they concluded that both K^+ and $H_2O_{interlayer}$ were not located in the prism's centers (a' and b' sites), as in the idealized model 2b, but rather in the center of the prism's faces. Gaillot et al. (2005) further refined this structure and showed that interlayer prisms contain three possible K sites, each shifted from the faces of the prism toward its center. Similar positions of interlayer cations were found for Cs^+-, Ba^{2+}-, and Sr^{2+}-exchanged KBi (Gaillot et al. in prep.). The Ca^{2+}-for-K^+ exchange in KBi modifies the initial layer stacking from the $3R_1$ polytype (model 2b) to the $1H$ one (model 1a). The driving force for the KBi-to-CaBi transformation is likely the possibility of forming strong H-bonds between $H_2O_{interlayer}$ providing octahedral coordination to Ca cations and O_{layer} of the adjacent layer (model 1a). Using mild hydrothermal conditions, Chen et al. (1996a) and Gaillot et
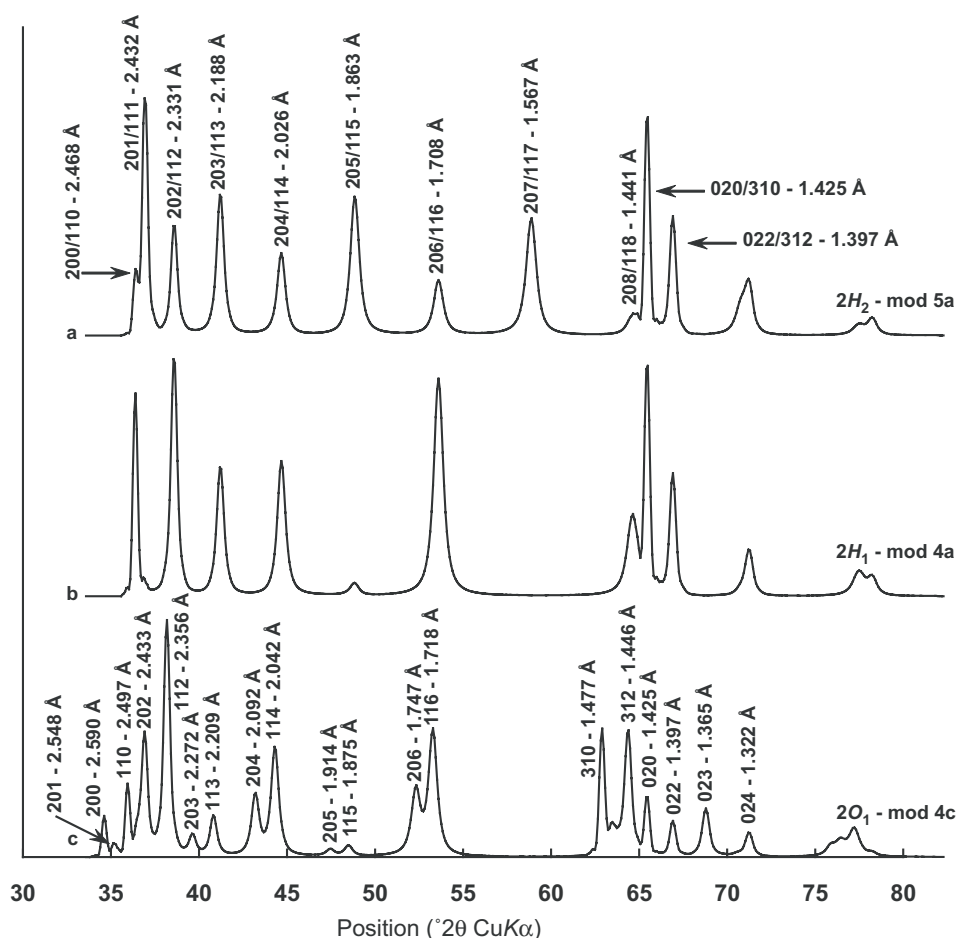
FIGURE 9. XRD patterns calculated for idealized structure models of birnessite polytypes. (**a**) $2H_2$ polytype with $Mn^{3+,2+}$ in ^{VI}TC position (Model 5a). (**b**) $2H_1$ polytype with $Mn^{3+,2+}$ in ^{VI}TC position (Model 4a). (**c**) $2O_1$ polytype with K^+ in the interlayer mid-plane (Model 4c).

al. (2005) synthesized directly Na-rich birnessite ($NaBi_h$) having a $3R_1$ unit cell. According to these authors, these $NaBi_h$ layers consist of Mn^{4+} cations and vacant octahedra but positions of interlayer Na^+ were not determined.

$2H_1$ Polytype. Kim et al. (1999) synthesized K-rich birnessite (KBi) from the decomposition of $KMnO_4$ at temperatures ranging from 200 to 1000 °C. Using the Rietveld technique, these authors showed that KBi obtained at 800 °C has two-layer hexagonal symmetry because of the regular alternation of octahedral layers rotated with respect to each other by 180° around the axis passing through layer Mn cations (polytype $2H_1$, model 4b). Gaillot et al. (2003) has shown that the actual structure of KBi obtained at 800 °C differs from the model of Kim et al. (1999) by several important details. First, KBi interlayers have heterogeneous cation composition with the coexistence of both K^+ and Mn^{3+} cations; second, because of the layer-to-interlayer migration of Mn^{3+} cations, KBi layers contain only Mn^{4+} cations and vacant octahedra. Finally, interlayer K^+ is not located in the prism's center. Rather K^+ is distributed over three possible sites, each of which being shifted from the center of the prism toward it faces. Thus, the idealized KBi structure corresponds to the coexistence of models 4a and 4b ($2H_1$ polytype).

$2O_1$ Polytype. KBi synthesized from the thermal decom-

position of $KMnO_4$ at 1000 °C has vacancy-free layers and orthogonal layer symmetry (polytype $2O_1$, model 5c—Gaillot et al. 2005, 2007).

Ambiguously determined polytypes. Kim et al. (2000) used the Rietveld technique to determine the structure of synthetic K-Li-rich birnessite (Li-K-Bi) obtained from the thermal decomposition of a Mn-KNO_3-$LiOH$ mixture at 800 and 1050 °C. They concluded that the 800 °C Li-K-Bi has a three-layer periodicity and hexagonal symmetry of layers, whereas the 1050 °C Li-K-Bi has an orthogonal layer symmetry and two-layer periodicity due to an ordered rotation of layers by 180°. However, the description of these structures was rather confusing because of technical errors. In particular, symbolic notations for the structures do not correspond to the proposed structure models. For example, the 1050 °C Li-K-Bi is described as AaB a' BbA b' instead of the actual notation given for model 4b (AcB a' BcA). In addition, unit-cell parameters given for the 1050 °C Li-K-Bi are not consistent with the proposed space group. Similarly, interatomic Mn-O distances differ significantly from those expected when heterovalent Mn_{layer} cations coexist within the octahedral layers. These authors also described the structure of the Li-K-Bi sample synthesized at 800 °C as AcB a' CbA c' BaC b' (model 3d, polytype $3R_2$), with octahedrally coordinated interlayer K^+
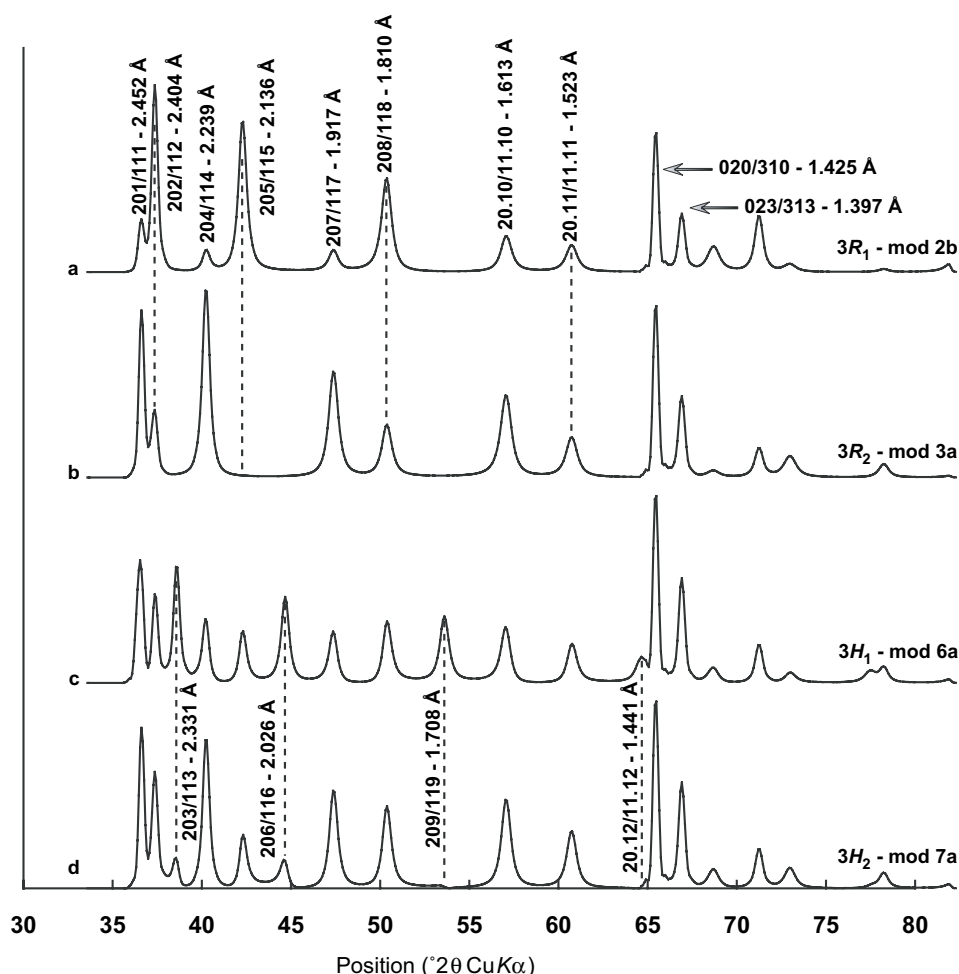
FIGURE 10. XRD patterns calculated for idealized structure models of birnessite polytypes. (**a**) $3R_1$ polytype with K^+ in the interlayer mid-plane (Model 2b). (**b**) $3R_2$ polytype with Zn^{2+} in ^{VI}TC position (Model 3a). (**c**) $3H_1$ polytype with $Mn^{3+,2+}$ in ^{VI}TC position (Model 6a). (**d**) $3H_2$ polytype with $Mn^{3+,2+}$ in ^{VI}TC position (Model 7a).

cations. However, atomic coordinates reported for this sample (Table 1—Kim et al. 2000) correspond to polytype $3R_1$ (model 2b) with interlayer K^+ having prismatic coordination. This latter structure model is consistent with the experimental XRD pattern reported for this sample (Fig. 4—Kim et al. 2000), which is similar to those obtained by Chen et al. (1996a) and Gaillot et al. (2005) from $3R_1$ polytypes (model 2b) synthesized under mild hydrothermal conditions. All these experimental patterns are similar to the one displayed on Figure 8a.

Turbostratic samples. Finally, one has to note that among different natural environments, and especially in soils, turbostratic birnessite is extremely common. For example, turbostratic birnessite has been reported as resulting from the bacterial oxidation of Mn^{2+} by different strains (Mandernack et al. 1995; Villalobos et al. 2003; Jurgensen et al. 2004; Bargar et al. 2005; Webb et al. 2005) and from abiotic processes (Mandernack et al. 1995). However, so far there is little unambiguous information derived from XRD data on the structure and crystal chemistry of these varieties. Most often the structural characterization of disordered birnessite is limited to the description of 00l peak positions as a function of relative humidity to assess the lamellar character of these "poorly crystalline birnessites." The position

of hkl reflections has also been used to hypothesize the actual layer symmetry (and thus the origin of the layer charge of these varieties) but without much experimental support (Villalobos et al. 2003; Jurgensen et al. 2004; Webb et al. 2005).

However, as described, birnessite having different layer symmetry may be unambiguously distinguished from each other from the shape of their hk bands (Fig. 12). A shoulder, resulting from the individualization of 20 and 11 reflections, is indeed visible on the low-angle side of the main maximum of the 20,11 band for orthogonal modifications (at ~2.55 and 2.45 Å, respectively—Fig. 12b), whereas this shoulder is logically absent for hexagonal modifications (Fig. 12a). Similarly, the 31,02 band of the orthogonal modifications contains two distinct maxima (~1.474 and 1.422 Å—Fig. 12b) which are merged for the hexagonal modifications (peak at ~1.422 Å—Fig. 12a). The features described for the orthogonal modifications are like those reported for the Mn oxides resulting from the oxidation of Mn^{2+} by *Bacillus sp.* strain SG-1 (Fig. 3 in Webb et al. 2005), indicating the presence of a high proportion of Mn^{3+} within the octahedral layers of this birnessite. The presence of Mn^{3+}-rich rows in vacancy-free layers, as in NaBi, is also supported by the splitting of the 8 Å^{-1} feature in the EXAFS spectra (Fig. 5 in
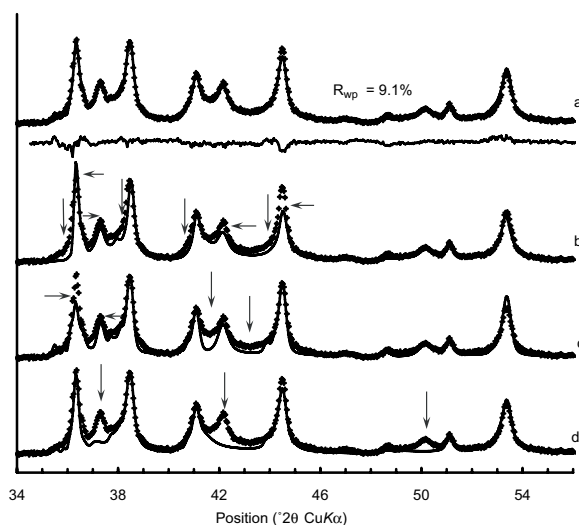
FIGURE 11. Comparison between experimental and calculated XRD patterns for a K-rich birnessite sample synthesized at 700 °C from the thermal decomposition of $KMnO_4$ (Gaillot et al. 2004). Experimental data are shown as crosses, whereas calculated profiles are shown as solid lines. Arrows outline the misfits between experimental and calculated patterns. Only 20*l* and 11*l* reflections are calculated. Atomic coordinates and other structural parameters used for the calculations as described by Gaillot et al. (2004). (**a**) Optimum model and difference plot. The optimum model includes contributions from a defect-free $2H_1$ polytype and from $2O_1/2H_1$, $2H_1/3R_1$, and $3R_1/2H_1$ mixed-layered structures (relative proportions 7:29:41:23). (**b**) Calculation made replacing the optimum $2O_1/2H_1$ contribution ($2O_1$:$2H_1$ ratio 50:50) by a defect-free $2H_1$ contribution. (**c**) Calculation made by subtracting the $2H_1/3R_1$ contribution ($2H_1$:$3R_1$ ratio 70:30) from the optimum model. (**d**) Calculation made by subtracting the $3R_1/2H_1$ contribution ($3R_1$:$2H_1$ ratio 90:10) from the optimum model. Adapted from Gaillot et al. (2004).
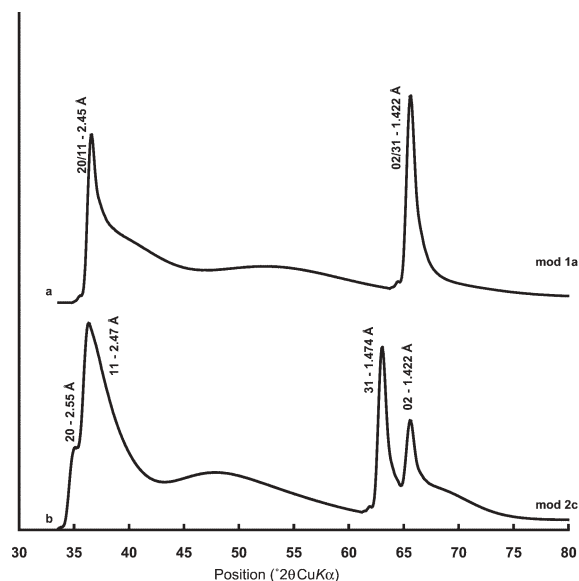
FIGURE 12. XRD patterns calculated for idealized structure models of turbostratic birnessite. (**a**) Birnessite with $Mn^{3+,2+}$ in ^{VI}TC position (Model 1a). (**b**) Birnessite with 0.67 Na^+ and $H_2O_{interlayer}$ in the interlayer mid-plane above below O_{layer} (Model 2c). Calculations were performed assuming a turbostratic stacking (100% random stacking faults). The radius of the coherent scattering domains in the **a-b** plane was set to 75 Å. All other parameters for XRD pattern calculations as described for Figure 5.

Webb et al. 2005) which has been described as characteristic of the presence of Mn^{3+}-rich rows in the octahedral Mn layer leading to its orthogonal symmetry (Fig. 9 in Gaillot et al. 2003; Fig. 6 in Marcus et al. 2004; Fig. 5 in Manceau et al. 2004; Manceau et al. 2005). To our knowledge, XRD patterns of all other turbostratic varieties reported so far in the literature correspond to hexagonal modifications.

In addition, Villalobos et al. (2006) demonstrated the high sensitivity of XRD profiles to the layer and interlayer structure of turbostratic phyllomanganates. In their study, Villalobos et al. (2006) observed contrasting experimental modulations of the 20,11 and 31,02 bands, and successfully reproduced them assuming a turbostratic stacking. In this case, the position and profile of the bands depend essentially on the amount and atomic coordinates of both layer and interlayer species, and these authors were able to determine the amount of vacant layer sites, as well as the amount and coordinates of both "heavy" ($Mn^{3+,2+}$) and "light" (Na^+, K^+, $H_2O_{interlayer}$) interlayer species. Such calculations also provided them with an estimate of the lateral extension of the octahedral layers (Drits and Tchoubar 1990; Jurgensen et al. 2004; Villalobos et al. 2006). The influence of the layer and interlayer structure on calculated profiles for 20,11 and 31,02 bands is illustrated in Figure 13. As compared to the structure model 1a (Fig. 13a), decreasing both the proportion of interlayer Mn and layer vacancies from 0.167 to 0.075 broadens the lineshape of the 20,11 and smoothes out the scattering dip at ~ 45 °2θ Cu$K\alpha$, thus rendering
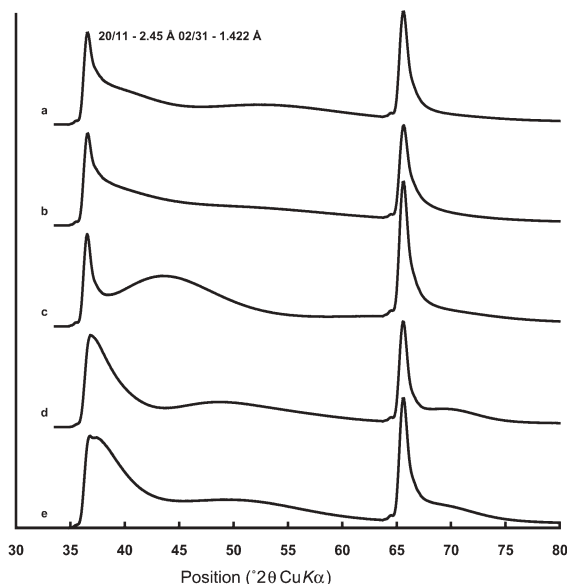

FIGURE 13. XRD patterns calculated for idealized structure models of turbostratic birnessite having hexagonal layer symmetry. (**a**) Birnessite with 0.833 vacant layer sites capped by $Mn^{3+,2+}$ in ^{VI}TC position (Model 1a). (**b**) Birnessite with 0.925 vacant layer sites capped by $Mn^{3+,2+}$ in ^{VI}TC position. (**c**) Birnessite with 0.833 vacant layer sites capped by $Mn^{3+,2+}$ in ^{VI}TE position (similar to Model 3d with interlayer $Mn^{3+,2+}$ cations). (**d**) Birnessite with 0.925 vacant layer sites and interlayer Na^+ (0.30 per octahedron) and H_2O molecules (0.90 per octahedron) in c' position (+1/3, 0, 1/2). (**e**) Birnessite with 0.925 vacant layer sites and interlayer K^+ (0.30 per octahedron) and H_2O molecules (0.90 per octahedron) in a' (–0.222, 0, 1/2) and c' (+1/3, 0, 1/2) positions, respectively. Calculations were performed as described for Figure 12.

the calculated hump at ~50–55 °2θ CuKα less pronounced (Fig. 13b). Moving interlayer Mn from the ^{VI}TC position dramatically modifies the 20,11 lineshape, as observed when the 0.167 interlayer Mn atoms are located above and/or below the tridentate cavities (^{VI}TE sites—Fig. 13c). The sensitivity of the 20,11 profile to the position of "light" interlayer species is illustrated next by assuming either the presence of Na$^+$ above and/or below O$_{layer}$ [(0.333, 0.0, 0.5)—Fig. 13d] or that of K$^+$ above/below the tridentate cavities [Position (–0.222, 0, 05) and equivalent positions—Fig. 13e], H$_2$O molecules sitting in both cases above and/or below O$_{layer}$. In the second case, the 20,11 band is broadened and the "hump" observed at ~50 °2θ CuKα in Figure 13d is both shifted toward higher angles and smoothened out. Similar modulations can however result from the partial ordering of the layer stacking (e.g., Ben Brahim et al. 1983, 1984; Drits and Tchoubar 1990; Viani et al. 2002). Special attention should thus be paid to the structural interpretation of these modulations, and, in this respect, verifying the structural XRD model with independent data from another structural technique, such as EXAFS spectroscopy, is always warranted.

ACKNOWLEDGMENTS

REFERENCES CITED

Aronson, B.J., Kinser, A.K., Passerini, S., Smyrl, W.H., and Stein, A. (1999) Synthesis, characterization, and electrochemical properties of magnesium birnessite and zinc chalcophanite prepared by a low-temperature route. Chemistry of Materials, 11, 949–957.
Bach, S., Henry, M., Baffier, N., and Livage, J. (1990) Sol-gel synthesis of manganese oxides. Journal of Solid State Chemistry, 88, 325–333.
Bach, S., Pereira-Ramos, J.-P., and Bafier, N. (1993) Electrochemical sodium insertion into the sol-gel birnessite manganese dioxide. Electrochimica Acta, 38, 1695–1698.
Bailey, S.W. (1980) Structures of layer silicates. In G.W. Brindley and G. Brown, Eds., Crystal Structures of Clay Minerals and their X-ray Identification, p. 1–123. Mineralogical Society, London.
——— (1988) Hydrous Phyllosilicates (exclusive of micas), 19, 725 p. Reviews in Mineralogy, Mineralogical Society of America, Chantilly, Virginia.
Bargar, J.R., Tebo, B.M., Bergmann, U., Webb, S.M., Glatzel, P., Chiu, V.Q., and Villalobos, M. (2005) Biotic and abiotic products of Mn(II) oxidation by spores of the marine *Bacillus sp*. strain SG-1. American Mineralogist, 90, 143–154.
Bartoli, C. (1997) Contribution à l'étude structurale des birnessites monocliniques saturées au potassium et au rubidium, 234 p. Ph.D. thesis, Orléans University, France.
Ben Brahim, J., Besson, G., and Tchoubar, C. (1983) Layer succession and water molecules arrangement in a homogeneous two-water layer Na-smectite. In J. Konta, Ed., 5th Meeting of the European Clay Groups, p. 65–75. Univerzita Karlova, Prague.
——— (1984) Etude des profils des bandes de diffraction X d'une beidellite-Na hydratée à deux couches d'eau. Détermination du mode d'empilement des feuillets et des sites occupés par l'eau. Journal of Applied Crystallography, 17, 179–188.
Bookin, A.S. and Drits, V.A. (1993) Polytype diversity of the hydrotalcite-like minerals. I. Possible polytypes and their diffraction features. Clays and Clay Minerals, 41, 551–557.
Burns, R.G. and Burns, V.M. (1977) The mineralogy and crystal chemistry of deep-sea manganese nodules, a polymetallic resource of the twenty-first century. Philosophical Transactions of the Royal Society of London (A), 286, 283–301.
Burns, V.M. and Burns, R.G. (1978) Post-depositional metal enrichment processes inside manganese nodules from the North Equatorial Pacific Ocean. Earth and Planetary Science Letters, 39, 341–348.
Chao, T.T. and Theobald, P.K. (1976) The significance of secondary iron and manganese oxides in geochemical exploration. Economic Geology, 71, 1560–1569.
Chen, R.J., Chirayil, T., Zavalij, P., and Whittingham, M.S. (1996a) The hydrothermal synthesis of sodium manganese oxide and a lithium vanadium oxide. Solid State Ionics, 86–88, 1–7.
Chen, R.J., Zavalij, P., and Whittingham, M.S. (1996b) Hydrothermal synthesis and

characterization of K$_x$MnO$_2$·yH$_2$O. Chemistry of Materials, 8, 1275–1280.
Ching, S. and Suib, S.L. (1997) Synthetic routes to microporous manganese oxides. Comments on Inorganic Chemistry, 19, 263–282.
Ching, S., Landrigan, J.A., Jorgensen, M.L., Duan, N., Suib, S.L., and O'Young, C.L. (1995) Sol-Gel synthesis of birnessite from KMnO$_4$ and simple sugars. Chemistry of Materials, 7, 1604–1606.
Ching, S., Petrovay, D.J., Jorgensen, M.L., and Suib, S.L. (1997a) Sol-Gel Synthesis of layered Birnessite-Type Manganese Oxides. Inorganic Chemistry, 36, 883–890.
Ching, S., Roark, J.L., Duan, N., and Suib, S.L. (1997b) Sol-Gel route to the tunneled manganese oxide cryptomelane. Chemistry of Materials, 9, 750–754.
Cho, J., Kim, G.B., Lim, H.S., Kim, C.-S., and Yoo, S.-I. (1999) Improvement of Structural Stability of LiMn$_2$O$_4$ Cathode Material on 55 °C Cycling by Sol-Gel Coating of LiCoO$_2$. Electrochemical and Solid-State Letters, 2, 607–609.
Chukhrov, F.V., Gorschkov, A.I., Rudnitskaya, E.S., and Sivtsov, A.V. (1978) Birnessite characterization. Izvestiya Akademie Nauk, SSSR, Seriya Geologicheskaya, 9, 67–76.
Chukhrov, F.V., Sakharov, B.A., Gorshkov, A.I., Drits, V.A., and Dikov, Y.P. (1985) Crystal structure of birnessite from the Pacific Ocean. International Geology Review, 27, 1082–1088.
Cornell, R.M. and Giovanoli, R. (1988) Transformation of hausmannite into birnessite in alkaline media. Clays and Clay Minerals, 36, 249–257.
Dachs, H. (1963) Neutronen- und Röntgenuntersuchungen am Manganit, MnOOH. Zeitschrift für Kristallographie, 118, 303–326.
Delmas, C., Fouassier, C., and Hagenmuller, P. (1980) Structural classification and properties of the layered oxides. Physica B, 99, 81–85.
Drits, V.A. (1987) Electron diffraction and high-resolution electron microscopy of mineral structures, 304 p. Springer Verlag, Berlin.
Drits, V.A. and Bookin, A.S. (2001) Crystal Structure and X-ray Identification of Layered Double Hydroxides. In V. Rives, Ed., Layered Double Hydroxides: Present and Future, p. 41–100. Nova Science Publishers, New York.
Drits, V.A. and McCarty, D.K. (1996) The nature of diffraction effects from illite and illite-smectite consisting of interstratified *trans*-vacant and *cis*-vacant 2:1 layers: A semi-quantitative technique for determination of layer-type content. American Mineralogist, 81, 852–863.
Drits, V.A. and Tchoubar, C. (1990) X-ray diffraction by disordered lamellar structures: Theory and applications to microdivided silicates and carbons, 371 p. Springer-Verlag, Berlin.
Drits, V.A., Petrova, V.V., and Gorshkov, A.I. (1985) Manganese minerals of Fe-Mn nodules from the sediments of the central part of Pacific Ocean and their postsedimentation transformation. Lithology and Raw Materials, 3, 17–39.
Drits, V.A., Silvester, E.J., Gorshkov, A.I., and Manceau, A. (1997a) The structure of monoclinic Na-rich birnessite and hexagonal birnessite. Part 1. Results from X-ray diffraction and selected area electron diffraction. American Mineralogist, 82, 946–961.
Drits, V.A., Srodon, J., and Eberl, D.D. (1997b) XRD measurement of mean crystallite tickness of illite and illite/smectite : Reappraisal of the Kubler index and the Scherrer equation. Clays and Clay Minerals, 45, 461–475.
Drits, V.A., Lanson, B., Gorshkov, A.I., and Manceau, A. (1998) Substructure and superstructure of four-layer Ca-exchanged birnessite. American Mineralogist, 83, 97–118.
Drits, V.A., Lanson, B., Bougerol Chaillout, C., Gorshkov, A.I., and Manceau, A. (2002) Structure of heavy-metal sorbed birnessite: Part 2. Results from electron diffraction. American Mineralogist, 87, 1646–1661.
Feng, Q., Kanoh, H., Miyai, Y., and Ooi, K. (1995) Hydrothermal synthesis of lithium and sodium manganese oxides and their metal ion extraction/insertion reactions. Chemistry of Materials, 7, 1226–1232.
Feng, Q., Sun, E.H., Yanagisawa, K., and Yamasaki, N. (1997a) Synthesis of birnessite-type sodium manganese oxides by solution reaction and hydrothermal methods. Journal of the Ceramic Society of Japan, 105, 564–568.
Feng, Q., Yanagisawa, K., and Yamasaki, N. (1997b) Synthesis of birnessite-type potassium manganese oxide. Journal of Materials Science Letters, 16, 110–112.
Gaillot, A.-C., Flot, D., Drits, V.A., Manceau, A., Burghammer, M., and Lanson, B. (2003) Structure of synthetic K-rich birnessite obtained by high-temperature decomposition of KMnO$_4$. I. Two-layer polytype from 800 °C experiment. Chemistry of Materials, 15, 4666–4678.
Gaillot, A.-C., Drits, V.A., Plancon, A., and Lanson, B. (2004) Structure of synthetic K-rich birnessites obtained by high-temperature decomposition of KMnO$_4$. 2. Phase and structural heterogeneities. Chemistry of Materials, 16, 1890–1905.
Gaillot, A.-C., Lanson, B., and Drits, V.A. (2005) Structure of birnessite obtained from decomposition of permanganate under soft hydrothermal conditions. 1. Chemical and structural evolution as a function of temperature. Chemistry of Materials, 17, 2959–2975.
Gaillot, A.-C., Drits, V.A., Lanson, B., and Manceau, A. (2007) Structure of synthetic K-rich birnessite obtained by high-temperature decomposition of KMnO$_4$. Structure of a two-layer polytype from 1000 °C experiments. Microporous and Mesoporous Materials, 98, 267–282.
Giovanoli, R., Stähli, E., and Feitknecht, W. (1970a) Über Oxidhydroxide des vierwertigen Mangans mit Schichtengitter. 1. Mitteilung: Natriummangan(II

,III)manganat(IV). Helvetica Chimica Acta, 53, 209–220.

——— (1970b) Über Oxidhydroxide des vierwertigen Mangans mit Schichten-gitter. 2. Mitteilung: Mangan(III)-manganat(IV). Helvetica Chimica Acta, 53, 453–464.

Glasser, L.S.D. and Ingram, L. (1968) Refinement of the crystal structure of Groutite, α-MnOOH. Acta Crystallographica, B24, 1233–1236.

Glover, E.D. (1977) Characterization of a marine birnessite. American Mineralogist, 62, 278–285.

Golden, D.C., Dixon, J.B., and Chen, C.C. (1986) Ion exchange, thermal transformations, and oxidizing properties of birnessite. Clays and Clay Minerals, 34, 511–520.

Gorshkov, A.I., Drits, V.A., Putilina, E.S., and Sivtsov, A.V. (1992) Natural and synthetic birnessites. Lithology and Raw Materials, 6, 12–23.

Herbstein, H.F., Ron, G., and Weissman, A. (1971) The thermal decompoition of Potassium Permanganate and related substances. Part I. Chemical aspects. Journal of the Chemical Society (A), 1821–1826.

Jurgensen, A., Widmeyer, J.R., Gordon, R.A., Bendell Young, L.I., Moore, M.M., and Crozier, E.D. (2004) The structure of the manganese oxide on the sheath of the bacterium *Leptothrix discophora*: An XAFS study. American Mineralogist, 89, 1110–1118.

Kim, S.H., Kim, S.J., and Oh, S.M. (1999) Preparation of layered MnO$_2$ via thermal decomposition of KMnO$_4$ and its electrochemical characterizations. Chemistry of Materials, 11, 557–563.

Kim, S.H., Im, W.M., Hong, J.K., and Oh, S.M. (2000) Factors controlling the stability of O3-and P2-type layered MnO$_2$ structures and spinel transition tendency in Li secondary batteries. Journal of the Electrochemical Society, 147, 413–419.

Kuma, K., Usui, A., Paplawsky, W., Gedulin, B., and Arrhenius, G. (1994) Crystal structures of synthetic 7 Å and 10 Å manganates substituted by mono- and divalent cations. Mineralogical Magazine, 58, 425–447.

Lanson, B., Drits, V.A., Silvester, E.J., and Manceau, A. (2000) Structure of H-exchanged hexagonal birnessite and its mechanism of formation from Na-rich monoclinic buserite at low pH. American Mineralogist, 85, 826–838.

Lanson, B., Drits, V.A., Feng, Q., and Manceau, A. (2002a) Structure of synthetic Na-birnessite: Evidence for a triclinic one-layer unit cell. American Mineralogist, 87, 1662–1671.

Lanson, B., Drits, V.A., Gaillot, A.-C., Silvester, E., Plancon, A., and Manceau, A. (2002b) Structure of heavy-metal sorbed birnessite: Part 1. Results from X-ray diffraction. American Mineralogist, 87, 1631–1645.

Le Goff, P., Baffier, N., Bach, S., and Pereira-Ramos, J.-P. (1994) Structural and electrochemical properties of layered manganese dioxides in relation to their synthesis: Classical and sol-gel routes. Journal of Materials Chemistry, 4, 875–881.

——— (1996) Synthesis, ion exchange and electrochemical properties of lamellar phyllomanganates of the birnessite group. Materials Research Bulletin, 31, 63–75.

Leroux, F., Guyomard, D., and Piffard, Y. (1995) The 2D rancieite-type manganic acid and its alkali-exchanged derivatives: Part I—Chemical characterization and thermal behavior. Solid State Ionics, 80, 299–306.

Ma, Y., Luo, J., and Suib, S.L. (1999) Syntheses of birnessites using alcohols as reducing reagents: Effects of synthesis parameters on the formation of birnessites. Chemistry of Materials, 11, 1972–1979.

Manceau, A. and Charlet, L. (1992) X-ray absorption spectroscopic study of the sorption of Cr(III) at the oxide-water interface. Journal of Colloid and Interface Science, 148, 425–442.

Manceau, A., Gorshkov, A.I., and Drits, V.A. (1992a) Structural Chemistry of Mn, Fe, Co, and Ni in Mn hydrous oxides. I. Information from XANES spectroscopy. American Mineralogist, 77, 1133–1143.

——— (1992b) Structural Chemistry of Mn, Fe, Co, and Ni in Mn hydrous oxides. II. Information from EXAFS spectroscopy, electron and X-ray diffraction. American Mineralogist, 77, 1144–1157.

Manceau, A., Drits, V.A., Silvester, E.J., Bartoli, C., and Lanson, B. (1997) Structural mechanism of Co^{2+} oxidation by the phyllomanganate buserite. American Mineralogist, 82, 1150–1175.

Manceau, A., Schlegel, M.L., Chateigner, D., Lanson, B., Bartoli, C., and Gates, W.P. (1999) Application of polarized EXAFS to fine-grained layered minerals. In D.G. Schulze, J.W. Stucki, and P.M. Bertsch, Eds., Synchrotron X-ray methods in clay science, 9, p. 68–114. Clay Minerals Society, Boulder, Colorado.

Manceau, A., Drits, V.A., Lanson, B., Chateigner, D., Wu, J., Huo, D., Gates, W.P., and Stucki, J.W. (2000a) Oxidation-reduction mechanism of iron in dioctahedral smectites: II. Crystal chemistry of reduced Garfield nontronite. American Mineralogist, 85, 153–172.

Manceau, A., Lanson, B., Drits, V.A., Chateigner, D., Gates, W.P., Wu, J., Huo, D., and Stucki, J.W. (2000b) Oxidation-reduction mechanism of iron in dioctahedral smectites: I. Crystal chemistry of oxidized reference nontronites. American Mineralogist, 85, 133–152.

Manceau, A., Lanson, B., Schlegel, M.L., Harge, J.-C., Musso, M., Eybert Berard, L., Hazemann, J.-L., Chateigner, D., and Lamble, G.M. (2000c) Quantitative Zn speciation in smelter-contaminated soils by EXAFS spectroscopy. American Journal of Science, 300, 289–343.

Manceau, A., Lanson, B., and Drits, V.A. (2002) Structure of heavy metal sorbed birnessite. Part III: Results from powder and polarized extended X-ray absorption fine structure spectroscopy. Geochimica et Cosmochimica Acta, 66, 2639–2663.

Manceau, A., Marcus, M.A., Tamura, N., Proux, O., Geoffroy, N., and Lanson, B. (2004) Natural speciation of Zn at the micrometer scale in a clayey soil using X-ray fluorescence, absorption, and diffraction. Geochimica et Cosmochimica Acta, 68, 2467–2483.

Manceau, A., Tommaseo, C., Rihs, S., Geoffroy, N., Chateigner, D., Schlegel, M., Tisserand, D., Marcus, M.A., Tamura, N., and Chen, Z.S. (2005) Natural speciation of Mn, Ni, and Zn at the micrometer scale in a clayey paddy soil using X-ray fluorescence, absorption, and diffraction. Geochimica et Cosmochimica Acta, 69, 4007–4034.

Mandernack, K.W., Post, J., and Tebo, B.M. (1995) Manganese mineral formation by bacterial spores of the marine *Bacillus*, strain SG-1: Evidence for the direct oxidation of Mn(II) to Mn(IV). Geochimica Et Cosmochimica Acta, 59, 4393–4408.

Marcus, M.A., Manceau, A., and Kersten, M. (2004) Mn, Fe, Zn and As speciation in a fast-growing ferromanganese marine nodule. Geochimica et Cosmochimica Acta, 68, 3125–3136.

Méring, J. (1949) L'interférence des rayons-X dans les systèmes à stratification désordonnée. Acta Crystallographica, 2, 371–377.

Norrestam, R. (1967) α-Manganese (III) oxide—A C-type sesquioxide of orthorhombic symmetry. Acta Chemica Scandinavica, 21, 2871–2884.

Paterson, E., Swaffield, R., and Clark, L. (1994) The influence of structure on Ba and K uptake by a synthetic phyllomangante. Clay Minerals, 29, 215–222.

Plançon, A. (2002) CALCIPOW—a program for calculating the diffraction by disordered lamellar structures. Journal of Applied Crystallography, 35, 377.

Post, J.E. and Veblen, D.R. (1990) Crystal structure determinations of synthetic sodium, magnesium, and potassium birnessite using TEM and the Rietveld method. American Mineralogist, 75, 477–489.

Shannon, R.D. (1976) Revised effective ionic radii and systematic studies of interatomic distances in halides and chalcogenides. Acta Crystallographica, A32, 751–767.

Shannon, R.D., Gumeman, P.S., and Chenavas, J. (1975) Effect of octahedral distortion on mean Mn^{3+}-O distances. American Mineralogist, 60, 714–716.

Silvester, E.J., Manceau, A., and Drits, V.A. (1997) The structure of monoclinic Na-rich birnessite and hexagonal birnessite. Part 2. Results from Chemical Studies and EXAFS Spectroscopy. American Mineralogist, 82, 962–978.

Stone, A.T., Godtfredsen, K.L., and Deng, B. (1994) Sources and reactivity of reductant encountered in aquatic environments. In G. Bidoglio and W. Stumm, Eds., Chemistry of aquatic systems: Local and global perspectives, p. 337–374. ECSC-EEC-EAEC, Brussels.

Tebo, B.M. and He, L.M. (1999) Microbially mediated oxidative precipitation reactions. In D.L. Sparks and T.J. Grundl, Eds., Mineral-water interfacial reactions, 715, p. 393–414. American Chemical Society, Washington, D.C.

Tebo, B.M., Bargar, J.R., Clement, B.G., Dick, G.J., Murray, K.J., Parker, D., Verity, R., and Webb, S.M. (2004) Biogenic manganese oxides: Properties and mechanisms of formation. Annual Review of Earth and Planetary Sciences, 32, 287–328.

Töpfer, J., Trari, M., Gravereau, P., Chaminade, J.P., and Doumerc, J.P. (1995) Crystal growth and reinvestigation of the crystal structure of crednerite, CuMnO$_2$. Zeitschrift für Kristallographie, 210, 184–187.

Tsuji, M., Komarneni, S., Tamaura, Y., and Abe, M. (1992) Cation exchange properties of a layered manganic acid. Materials Research Bulletin, 27, 741–751.

Tu, S., Racz, G.J., and Goh, T.B. (1994) Transformations of synthetic birnessite as affected by pH and manganese concentration. Clays and Clay Minerals, 42, 321–330.

Viani, A., Gaultieri, A.F., and Artioli, G. (2002) The nature of disorder in montmorillonite by simulation of X-ray powder patterns. American Mineralogist, 87, 966–975.

Villalobos, M., Toner, B., Bargar, J., and Sposito, G. (2003) Characterization of the manganese oxide produced by Pseudomonas putida strain MnB1. Geochimica et Cosmochimica Acta, 67, 2649–2662.

Villalobos, M., Lanson, B., Manceau, A., Toner, B., and Sposito, G. (2006) Structural model for the biogenic Mn oxide produced by Pseudomonas putida. American Mineralogist, 91, 489–502.

Webb, S.M., Tebo, B.M., and Bargar, J.R. (2005) Structural characterization of biogenic Mn oxides produced in seawater by the marine *Bacillus sp*. strain SG-1. American Mineralogist, 90, 1342–1357.

Yang, D.S. and Wang, M.K. (2001) Syntheses and characterization of well-crystallized birnessite. Chemistry of Materials, 13, 2589–2594.